AGU PUBLICATIONS

JGR

Journal of Geophysical Research: Solid Earth

RESEARCH ARTICLE
10.1002/2016JB013361

Key Points:
- New GPS, hydrological, and GRACE data pointing to a previously unnoticed transient deformation signal of karst aquifers in southern Apennines
- Horizontal signal is controlled by seasonal and multiyear phases of groundwater recharge/discharge of karst aquifers
- Vertical component is closely correlated with estimates of total water storage from GRACE satellite mission

Supporting Information:
- Supporting Information S1
- Table S1

Correspondence to:
F. Silverii,
francesca.silverii@ingv.it

Citation:
Silverii, F., N. D'Agostino, M. Métois, F. Fiorillo, and G. Ventafridda (2016), Transient deformation of karst aquifers due to seasonal and multiyear groundwater variations observed by GPS in southern Apennines (Italy), *J. Geophys. Res. Solid Earth*, *121*, 8315–8337 doi:10.1002/2016JB013361.

Received 15 JUL 2016
Accepted 1 NOV 2016
Accepted article online 7 NOV 2016
Published online 14 NOV 2016

Transient deformation of karst aquifers due to seasonal and multiyear groundwater variations observed by GPS in southern Apennines (Italy)

Francesca Silverii[1,2], Nicola D'Agostino[1], Marianne Métois[1,3], Francesco Fiorillo[4], and Gerardo Ventafridda[5]

[1]Istituto Nazionale di Geofisica e Vulcanologia, Centro Nazionale Terremoti, Rome, Italy, [2]Dipartimento di Fisica, Settore di Geofisica, University "Alma Mater Studiorum", Bologna, Italy, [3]Laboratoire de Géologie (LGLTPE), Claude Bernard – Lyon University, Lyon, France, [4]Dipartimento di Scienze e Tecnologie, University of Sannio, Benevento, Italy, [5]Acquedotto Pugliese S.p.A., Bari, Italy

Abstract We present GPS, hydrological, and GRACE (Gravity Recovery and Climate Experiment) observations in southern Apennines (Italy) pointing to a previously unnoticed response of the solid Earth to hydrological processes. Transient patterns in GPS horizontal time series near to large karst aquifers are controlled by seasonal and interannual phases of groundwater recharge/discharge of karst aquifers, modulating the extensional ~3 mm/yr strain within the tectonically active Apennines. We suggest that transient signals are produced, below the saturation level of the aquifers and above a poorly constrained depth in the shallow crust, by time-dependent opening of subvertical, fluid-filled, conductive fractures. We ascribe this process to the immature karstification and intense tectonic fracturing, favoring slow groundwater circulation, and to multiyear variations of the water table elevation, influenced by variable seasonal recharge. The vertical component displays seasonal and multiyear signals more homogeneously distributed in space and closely correlated with estimates of total water storage from GRACE, reflecting the elastic response of the lithosphere to variations of surface water loads. The different sensitivities of vertical and horizontal components to the hydrologically induced deformation processes allow us to spatially and temporally resolve the different phases of the water cycle, from maximum hydrological loading at the surface to maximum hydrostatic pressure beneath karst aquifers. Finally, we suggest that transient deformation signals in the geodetic series of the Apennines are correlated to large-scale climatic patterns (Northern Atlantic Oscillation) through their influence on precipitation variability and trends at the regional scale.

1. Introduction

It is well known that redistribution of water masses in the shallow crust of the Earth affects surface measurements of crustal displacement. Early studies of hydrologically related deformation have initially used measurements obtained by theodolites, strainmeters, tiltmeters, and extensometers [e.g., *Edge et al.*, 1981; *Wolfe et al.*, 1981; *Evans and Wyatt*, 1984]. In the last 20 years space geodesy has revolutionized the surveying and measurement of crustal deformation. In particular, continuously operating Global Positioning System (cGPS) networks are used to derive station positions with typical daily repeatability of 1–2 mm for horizontal positions and 3–4 mm for vertical positions [*Blewitt et al.*, 2013]. Thanks to their high-accuracy, geographic distribution, and temporal continuity, space geodesy observations are providing important contributions to the study of hydrological processes in different aquifer systems and geological environments [e.g., *Zhang et al.*, 2012; *Argus et al.*, 2014; *Borsa et al.*, 2014; *Chanard et al.*, 2014].

The response of Earth's crust to water content variations is generally described in terms of two end-member models. In the first model the observed deformation is explained as the elastic response of the Earth to hydrological surface loading [*Farrell*, 1972]. Most studies have focused on the vertical component of the deformation, since horizontal displacements induced by surface loading tend to be much smaller than vertical displacements [*Wahr et al.*, 2013]. As an example, this approach has been successfully used to explain the uplift associated to the recent drought affecting the Western USA [e.g., *Amos et al.*, 2014; *Argus et al.*, 2014; *Borsa et al.*, 2014]. In the second model, the theory of poroelasticity [e.g., *Wang*, 2000] is generally used to explain

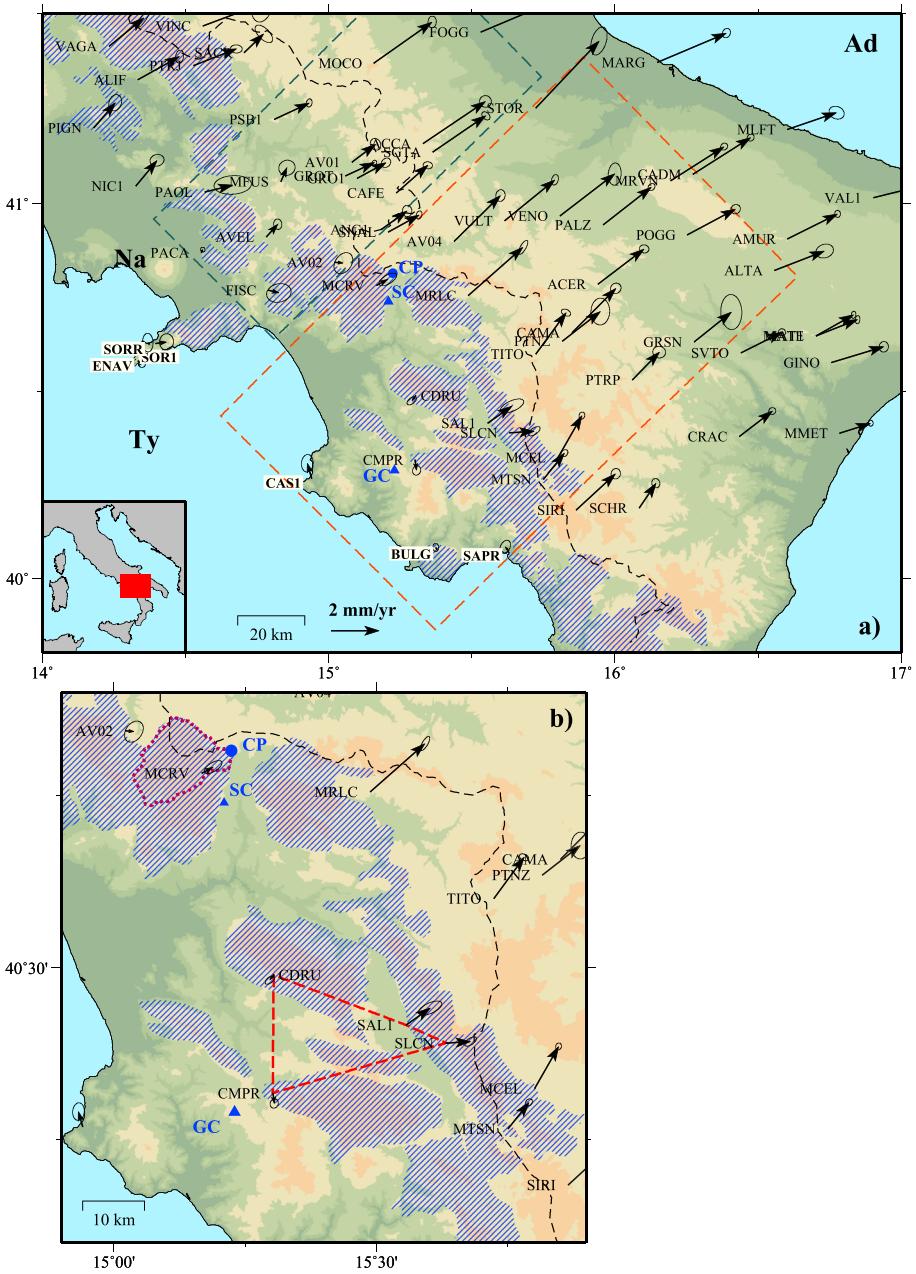

Figure 1. (a) General framework of the study area (red rectangle in the inset). Black vectors represent GPS horizontal interseismic velocities in a Tyrrhenian reference frame with 95% CI ellipses. The name of GPS sites used to define this frame are highlighted in white. The black dashed line indicates the drainage divide; the blue striped areas outline the main carbonate aquifers; the blue circle indicates the location of Caposele (CP) spring; and the blue triangles show Senerchia (SC) and Gioi Cilento (GC) rain gauges positions. The dashed orange and dark-grey boxes include the GPS sites whose time series are represented, respectively, in Figures 2 and 5. (b) Zoomed portion of the carbonate area: the red dashed line delineates the polygon in which dilatational strain shown in Figure 4 is calculated; the brown dotted line defines the Caposele spring catchment area.

the deformation of alluvial and basin-fill aquifers. In this case the groundwater flow is governed by primary porosity and the surface responds with subsidence and horizontal contraction to groundwater extraction [e.g., *Galloway and Burbey*, 2011] or uplift and horizontal expansion to water table increase [e.g., *King et al.*, 2007].

In this work we describe a hydrologically related, multiyear transient signal in GPS time series of south-central Italy (Figure 1) related to the deformation of karst aquifers. The latter have complex features that make them

dissimilar from other aquifers [*Bakalowicz*, 2005]. Differently from granular aquifers (e.g., alluvial aquifers), where porosity is mostly due to spaces between the grains, karst aquifers are bodies of soluble rock, typically carbonate rock, usually characterized by enhanced, secondary porosity (e.g., conduits, caves, and fissures) formed by the dissolution of the rock. Previous studies of hydrologically related deformation of karst aquifers have revealed transient signals following large rainfall events. Such signals have been ascribed to the opening of hydrologically active fractures/conduits located nearby ($\sim 10^0$ km) of the measuring instruments (e.g., tiltmeters), in the epikarst, or the vadose zone of the aquifer (depth $\sim 10^2$ m) [*Evans and Wyatt*, 1984; *Guglielmi et al.*, 2008; *Longuevergne et al.*, 2009; *Jacob et al.*, 2010; *Tenze et al.*, 2012; *Amoruso et al.*, 2014]. In a recent paper *Devoti et al.* [2015] highlighted a rain-correlated deformation at the Cansiglio Plateau (CP) karst region (northern Italy) affecting mainly the horizontal component of GPS time series of the area, with nearly no effects on the vertical component. Given the high correlation with events of heavy rainfall, the authors ascribe the deformation episodes to active fracture expansion in the vadose zone. In the southern Apennines, karst aquifers originate from thick Mesozoic carbonate massifs, generally hydraulically isolated by marly-arenaceous Neogene sequences or other nonkarstic less permeable rocks along their boundaries. The absence of recent moderate to large earthquakes, a dense continuous GPS network with more than 10 years of data at several stations and the presence of large calcareous ridges able to store a huge quantity of water [e.g., *Fiorillo et al.*, 2015b] provide a relevant opportunity to study the deformation response of large karst aquifers (in terms of magnitude, depth, and timing) to time-dependent climatic variability and aquifer recharge conditions. This is particularly interesting due to the role of karst aquifers as a significant global resource of freshwater at both national [e.g., *Fiorillo et al.*, 2015b] and global [*Hartmann et al.*, 2014] scales.

We analyze horizontal and vertical GPS time series integrated with rainfall data, karst spring discharge time series and estimates of equivalent water height data from the Gravity Recovery and Climate Experiment (GRACE) satellites. The paper is structured as follows: first, we separately present GPS (section 2) and hydrological (section 3) data. In the following sections, we analyze the correlations between geodetic and hydrological signals (sections 3.4 and 4), and we discuss the results and investigate the processes responsible for the observed response of the solid Earth to the different phases of the water cycle (section 5).

2. GPS Data and Analysis

In this work we use daily observations from permanent GPS stations in the southern Apennines, most of which belong to the Rete Integrata Nazionale GPS network (RING) (http://ring.gm.ingv.it [*Avallone et al.*, 2010]). Site coordinates of stations from RING and other networks can be found in the supporting information (Table S1).

We reduce GPS data by using the Jet Propulsion Laboratory (JPL) GIPSY-OASIS II software (version 6.2) in a Precise Point Positioning mode applied to ionospheric-free carrier phase and pseudorange data [*Zumberge et al.*, 1997] and using JPL's final fiducial-free GPS orbit products. We apply the Global Pressure and Temperature model 2 (GPT2) tropospheric mapping function [*Lagler et al.*, 2013] and estimate tropospheric wet zenith delay and horizontal gradients as stochastic random-walk parameters every 5 min [*Bar-Sever et al.*, 1998] in order to model tropospheric refractivity. We compute the ocean loading from the FES2004 tidal model [*Scherneck*, 1991] coefficients provided by the Ocean Tide Loading Provider (http://holt.oso.chalmers.se/loading) and apply it as a station motion model. We apply the ambiguity resolution by using the wide lane and phase bias method [*Bertiger et al.*, 2010].

In order to analyze and interpret station velocities relative to the Eurasian plate and to reduce the common mode signal, we adopt the Eurasian terrestrial reference frame described in *Métois et al.* [2015]. This frame is defined by six Cartesian coordinates and velocities of each of 174 stations selected by specific quality criteria. Our Eurasian frame is aligned in origin and scale with International GNSS Service 2008 (IGS08) [*Rebischung et al.*, 2012] and implemented to have no-net rotation with respect to the Eurasian plate, realized by minimizing the horizontal velocities of 69 stations located in the stable interior of the plate. We obtain GPS velocities and associated uncertainties by fitting a linear trend plus annual and semiannual terms and site specific offsets to position time series, assuming a white + flicker noise stochastic model [*Williams*, 2008].

In order to emphasize the long-term, secular ~3 mm/yr NE-SW directed active extension across the Apennines, we show crustal velocities in Figure 1 by using a Tyrrhenian reference frame, obtained by minimizing horizontal velocities of stations on the Tyrrhenian coast [*D'Agostino*, 2014]. We exclude stations possibly affected by ongoing volcanic deformation near Naples (Vesuvio and Campi Flegrei). We show the time series of vertical and horizontal components (rotated in a N45E and N135E directions, respectively, perpendicular and

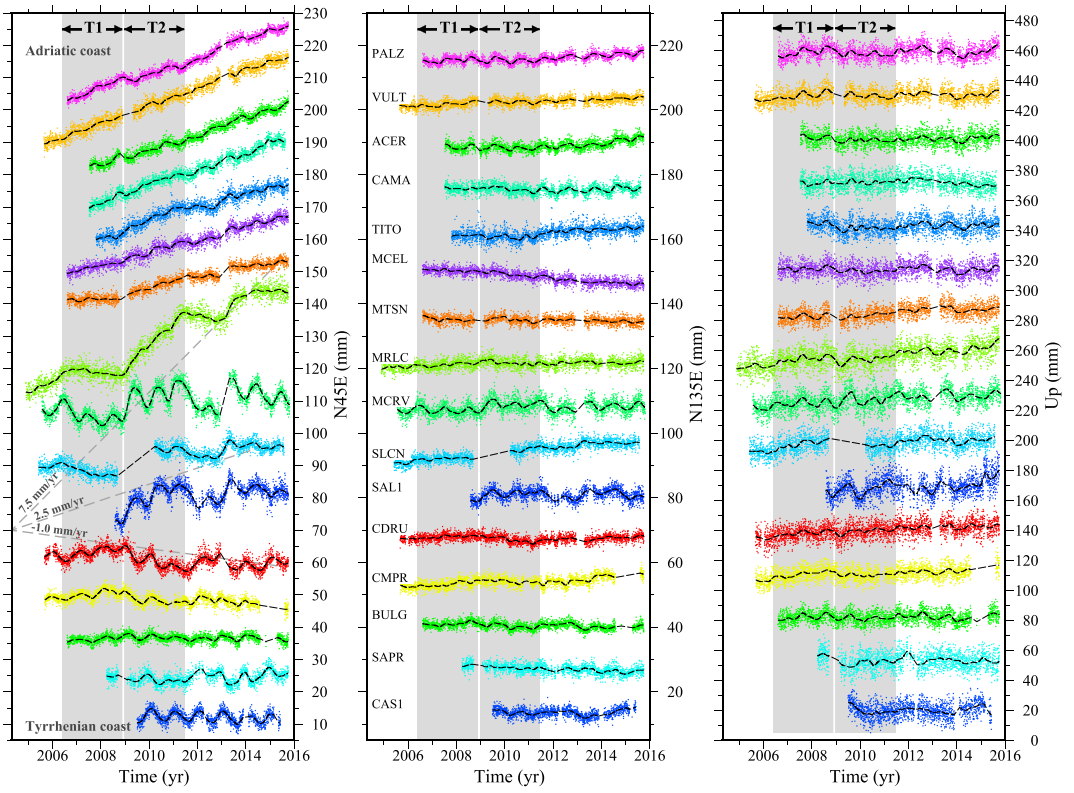

Figure 2. Observed (colored dots) time series for sites included in the dashed orange rectangle of Figure 1a. Black dashed lines represent a 6 month Gaussian filter of the time series (i.e., the weights are given by the Gaussian function, and the width is 6 times the conventional Gaussian sigma). GPS sites are ordered from the Tyrrhenian coast (bottom) toward the Adriatic coast (top). (left) Horizontal component projected along a direction perpendicular to the long axis of the Apennines (N45E). (center) Horizontal component projected along a direction parallel to the long axis of the Apennines (N135E). (right) Vertical component. T1 and T2 refer to the two time intervals in which velocities represented in Figure 3 are calculated.

parallel to the long axis of the Apennines) in Figure 2, progressively ordered from the Tyrrhenian (to the west) to the Adriatic (to the east) coasts. These time series show that the interseismic ~3 mm/yr extensional opening in the axial part of the Apennines [*D'Agostino*, 2014] is modulated by annual and multiyear (~4 years) signals that modify the intensity of the tectonic signal. This is clearly visible in the N45E horizontal component, whereas the N135E component (i.e., the component of the velocity that is parallel to the mountain belt) shows only a reduced signal strength (Figure 2). Both the annual and multiyear horizontal signals show consistent spatial patterns displaying a symmetrical behavior with respect to an axis running along the crest of the Apennines. With respect to this axis of symmetry, both the annual and multiyear transient signals display episodes of opposed enhanced or reduced secular motion (see for instance the behavior of stations SAL1 and CDRU, located on opposite sides of the karst aquifer, in Figure 2). In Figure 2 we highlight two multiyear episodes (each 2.5 year long) of inward (T1, 2006.4–2008.9) and outward (T2, 2008.95–2011.45) motion of the stations in the axial part of the Apennines. The effect of such episodes stands out clearly in the time series as notable deviations from the ~2006–2016 trend. Accordingly, we fit a trend with annual and semiannual periodicities, assuming a white + flicker noise (CATS software by *Williams* [2008]) to GPS horizontal components for each T1 and T2 interval, subtracting the resulting values from the long-term (~2006–2016) trends. These deviations from the 2006–2016 trend are displayed in Figure 3, clearly showing the transient shortening/extensional T1/T2 episodes in the axial part of the Apennines.

The time evolution of the strain due to the relative motion of the sites crossing the symmetry axis (polygon in Figure 1b formed by CMPR, CDRU, SAL1, SLCN) clearly illustrates the deviations from a steady state strain accumulation. Relative to the long-term extensional signal of ≈70 nstrain/year, the previously defined T1, T2 episodes correspond to reduced or negative dilatation rate (T1, ≈ −30 nstrain/year) or enhanced dilatational rate (T2, ≈150 nstrain/year) (Figures 4a and 4b). Since this positive/negative enhancement of extensional

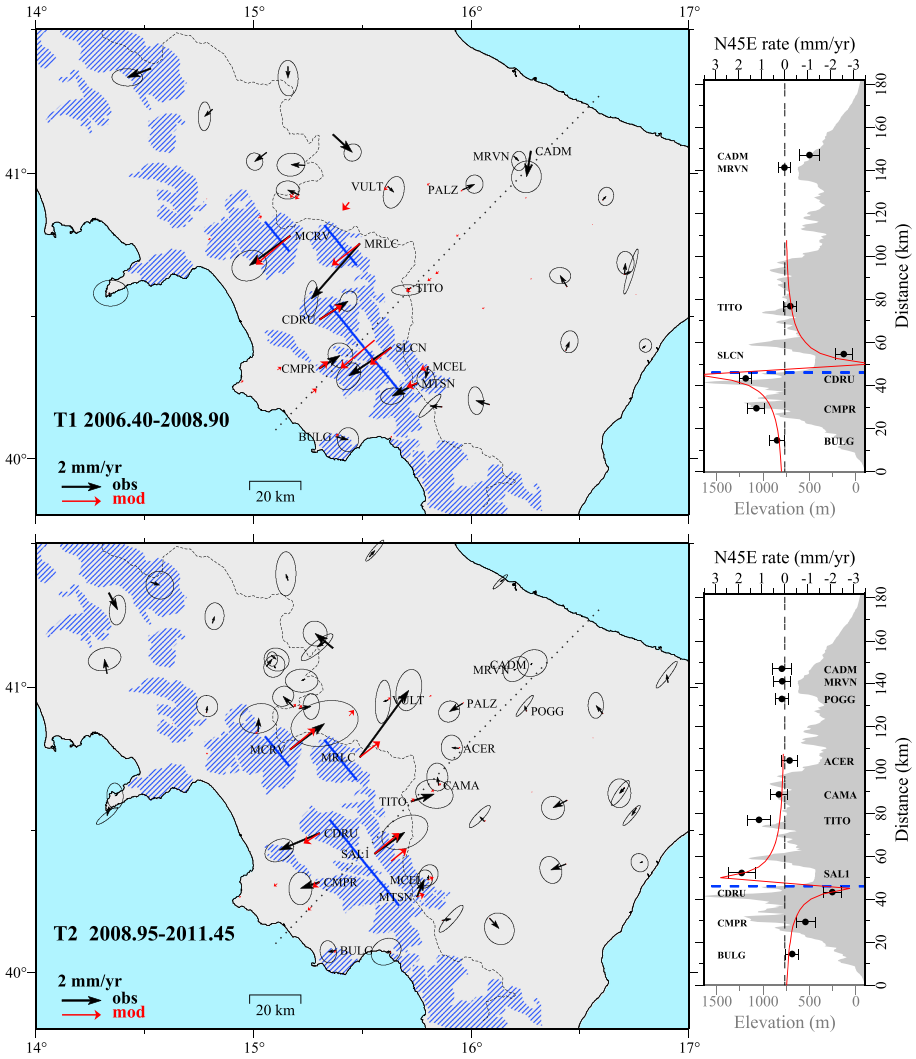

Figure 3. Observed (black, with 95% CI ellipses) and modeled (red) GPS velocities calculated as deviation from the long-term trend (top) in a period of decreasing precipitation and karst aquifer exhaustion (T1) and (bottom) in a period of increasing precipitation and aquifer recharge (T2). Modeled rates are calculated from the best fit model shown in Figure 13. The thick blue lines indicate the position of the vertical tensile dislocations used in the model. The plots on the right side represent the cross sections along the dotted lines on the maps: topography (grey area), observed rates (black circles with error bars), modeled rates along the profile (red line), and position of the dislocation (vertical dashed blue line).

strain is confined in the center of the Apennines, the long-term overall extension across the Apennines is approximately steady.

Figure 3 shows that the stations affected by significant deviations from the 2006–2016 trend are not homogeneously distributed but are preferentially located close to the limestone mountain ridges hosting large karst aquifers [*Allocca et al.*, 2007, 2014]. Stations far from calcareous lithologies (as most of the stations included in the dark-grey dashed line box in Figure 1 and the ones on the Adriatic side in the orange dashed line box in Figure 1) do not display a clear evidence of such multiyear transient deformation in the horizontal components (Figures 2, 3, and 5). This spatial correlation with karst formations (Figure 3) led us to look after hydrological processes that could explain the observed transients.

A low signal-to-noise ratio in vertical time series obscures clear patterns of vertical multiyear signals at individual stations (Figures 2 and 5). A simple approach to recover spatially and temporally consistent signals is to stack the daily values of detrended vertical time series for several selected stations with long and good records

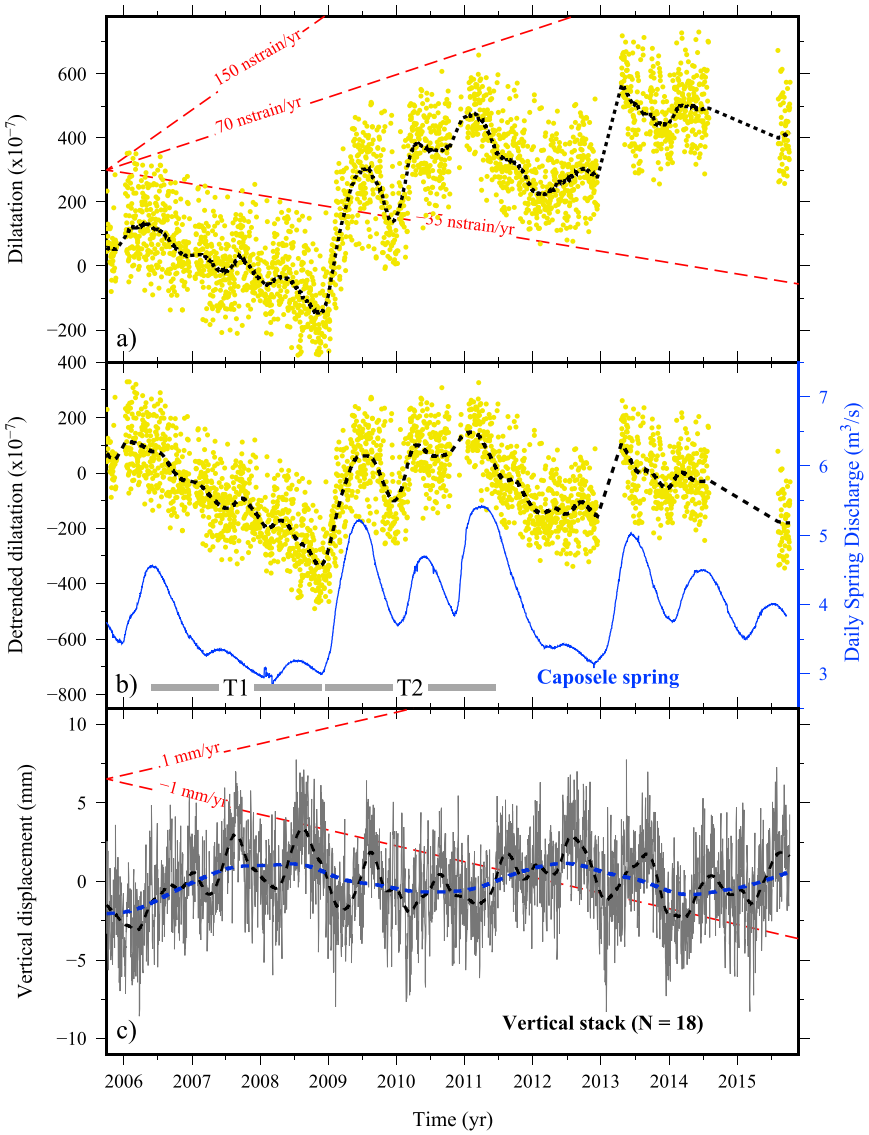

Figure 4. (a) Daily dilatation values calculated in the polygon represented in Figure 1b (yellow dots) and its 6 month Gaussian filter (black dashed line). (b) Detrended dilatation time series and daily discharge data of Caposele spring (blue line). (c) Vertical daily time series obtained by stacking data from 18 stations (grey line) and its 6 month (black dashed line) and 2.5 year (blue dashed line) Gaussian filters. T1 and T2 time intervals highlighted in Figure 2 are also shown. Reference trends (red dashed lines) in Figures 4a and 4c emphasize the sustained episodes of deviation from decadal trends. *N* is the number of GPS sites used to compute the stacked series.

in the study area (ACCA, ACER, BULG, CAFE, CAMA, CDRU, CMPR, FOGG, GROT, MCEL, MCRV, MRLC, MTSN, PALZ, PSB1, SGTA, SLCN, and VULT). The results of the stacking analysis confirm that a consistent seasonal signal exists in the vertical component (maximum downward motion in January–February and maximum uplift in July–August). We also observe two peaks of multiyear downward motion in 2010–2011 and 2014, which are clearly visible by applying a low-pass 2.5 year Gaussian filter to the daily vertical stacked series (Figure 4c). With this kind of filter, the weights are given by the Gaussian function and the width is 6 times the conventional Gaussian sigma. In order to verify if noticeable differences exist between the vertical signal inside and outside the karst area, we compute separate vertical stacks using stations inside (BULG, CMPR, CDRU, MCRV, MRLC, MTSN, MCEL, and SLCN) and outside (ACCA, ACER, CAFE, CAMA, FOGG, GROT, PALZ, PSB1, SGTA, and VULT) the karst area (Figure 6). In contrast to what we observe for the horizontal component, the behavior of the vertical component does not show significant differences between the two groups of stations at both the seasonal and multiyear scales.

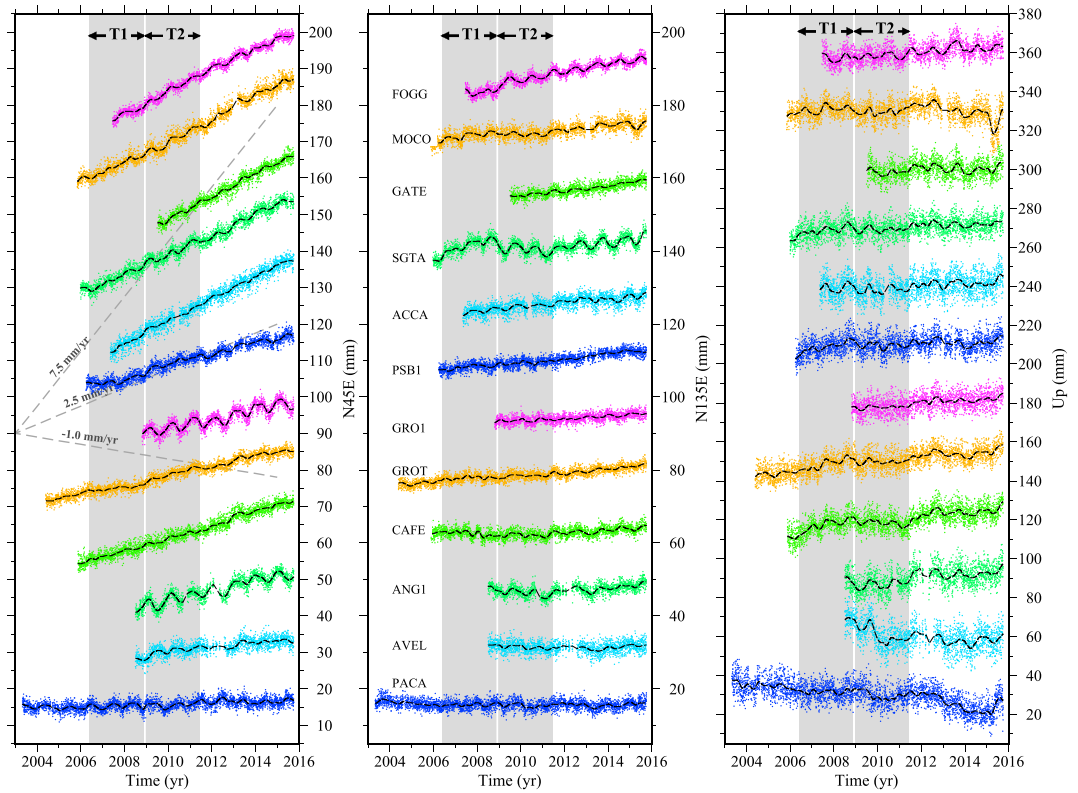

Figure 5. Observed time series of sites included in the dashed dark-grey rectangle in Figure 1a. Black dashed lines represent 6 month Gaussian filters. GPS sites are ordered from Tyrrhenian coast (bottom) toward Adriatic coast (top). (left) Horizontal component projected along a direction perpendicular to the long axis of the Apennines (N45E). (center) Horizontal component projected along a direction parallel to the long axis of the Apennines (N135E). (right) Vertical component. Notice the absence of the significant varying annual and multiyear signals observed in the N45E component of Figure 2.

The comparison of horizontal and vertical stack time series show that, at the multiyear scale, episodes of inward horizontal motion and reduced axial extensional strain (T1) in the karst area are roughly associated with general upward motion; the reverse occurs during episodes of outward motion (T2) (Figures 4 and 7). At the annual scale, the peaks of seasonal downward motion, occurring in late fall-winter (vertical blue reversed arrows in Figure 7b), precede by ≈5–6 months the peaks of maximum positive horizontal dilatational strain (emphasized in Figure 7a with red vertical dashed lines and diverging arrows).

It has been shown that atmospheric pressure loading (ATML) causes deformation of the surface of the Earth which especially affects the vertical component [*Tregoning and van Dam*, 2005]. We attempt to mitigate the ATML effects on the GPS height estimates using the data and programs provided by the Global Geophysical Fluid Center (GGFC) [*van Dam*, 2010]. The GGFC solution is 6 h and global surface displacement at 2.5° × 2.5° spacing determined from the National Center for Environmental Protection reanalysis surface pressure. We calculate daily-averaged atmospheric loading corrections and remove them from the GPS solutions as a post-processed correction to the vertical component in the CM frame (center of mass of the total Earth). Correcting for ATML increases the variance of heights for the sites included in the computation of the vertical stack without resulting in significant variations of the vertical component behavior and maintaining the homogeneity between sites inside and outside the karst area. Therefore, given the results of *Valty et al.* [2015], pointing to a dominant role of hydrological loads in controlling vertical displacements in Southern Europe, we only consider and show the results without the atmospheric correction.

3. Hydrological Data

The Mediterranean climatic features and their temporal variability strongly control the amount of surface water and the recharge processes of the karst aquifers in southern Apennines. Large-scale atmospheric

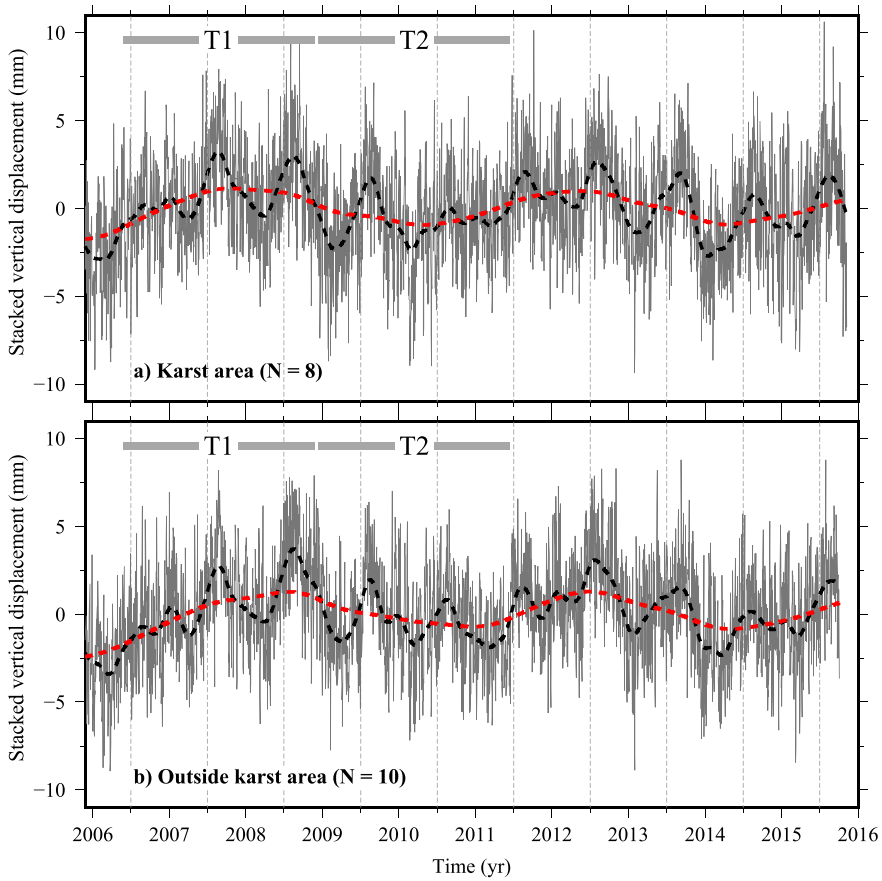

Figure 6. Comparison between vertical stacked time series computed by using selected sites (a) in the karst aquifers area and (b) outside the karst aquifers area. The black dashed lines represent a 6 month Gaussian filter, the red dashed lines represent a 2.5 year Gaussian filter. T1 and T2 time intervals highlighted in Figure 2 are also shown. *N* is the number of GPS sites used to compute the stacked series.

circulation patterns explain much of the variability and trends in precipitation and temperature at the regional scale. Similarly to other Mediterranean mountainous regions, winter precipitation and temperature variability are influenced by the North Atlantic Oscillation (NAO) [*Hurrell et al.*, 2001; *De Vita et al.*, 2012; *López-Moreno et al.*, 2011]. The NAO is characterized by a spatial dipole, with pressure anomaly centers located near the Azores and near Iceland [*Hurrell*, 1995]. During positive (negative) phases both pressure centers are reinforced (weakened) and displaced to the south (north). The location of the pressure centers markedly affects precipitation and temperature across large parts of Europe and the Mediterranean regions [*Hurrell and van Loon*, 1997; *Wanner et al.*, 2001; *Álvarez García et al.*, 2012].

The spatial distribution of the mean annual precipitation is mainly influenced by the orographic effect of the Apennines on humid air masses moving eastward from the Tyrrhenian Sea. Higher orographic precipitation occurs in the western sector, with maximum cumulative annual values up to 1700–2000 mm along the ridge itself and lower precipitations down to 700–900 mm east of the Apennines [*Allocca et al.*, 2014].

Here we present three different kinds of observables that provide information about hydrological phenomena: the rain gauge data, the discharge data of one of the main karst springs of Southern Italy, and the measurements of the terrestrial water storage variations obtained by the GRACE mission.

3.1. Rainfall Data

Annual precipitation in the study area ranges between 1000 and more than 2000 mm (at the highest elevations). Rainfall typically reaches a maximum during November and a minimum in July [*Fiorillo*, 2009; *Allocca et al.*, 2014]. We consider daily time series of rainfall data from two rain gauges (Gioi Cilento and Senerchia) from Protezione Civile Regione Campania (http://centrofunzionale.regione.campania.it/index.php/rete-di-monitoraggio). Thanks to their record completeness and location, we assume that these rain gauges

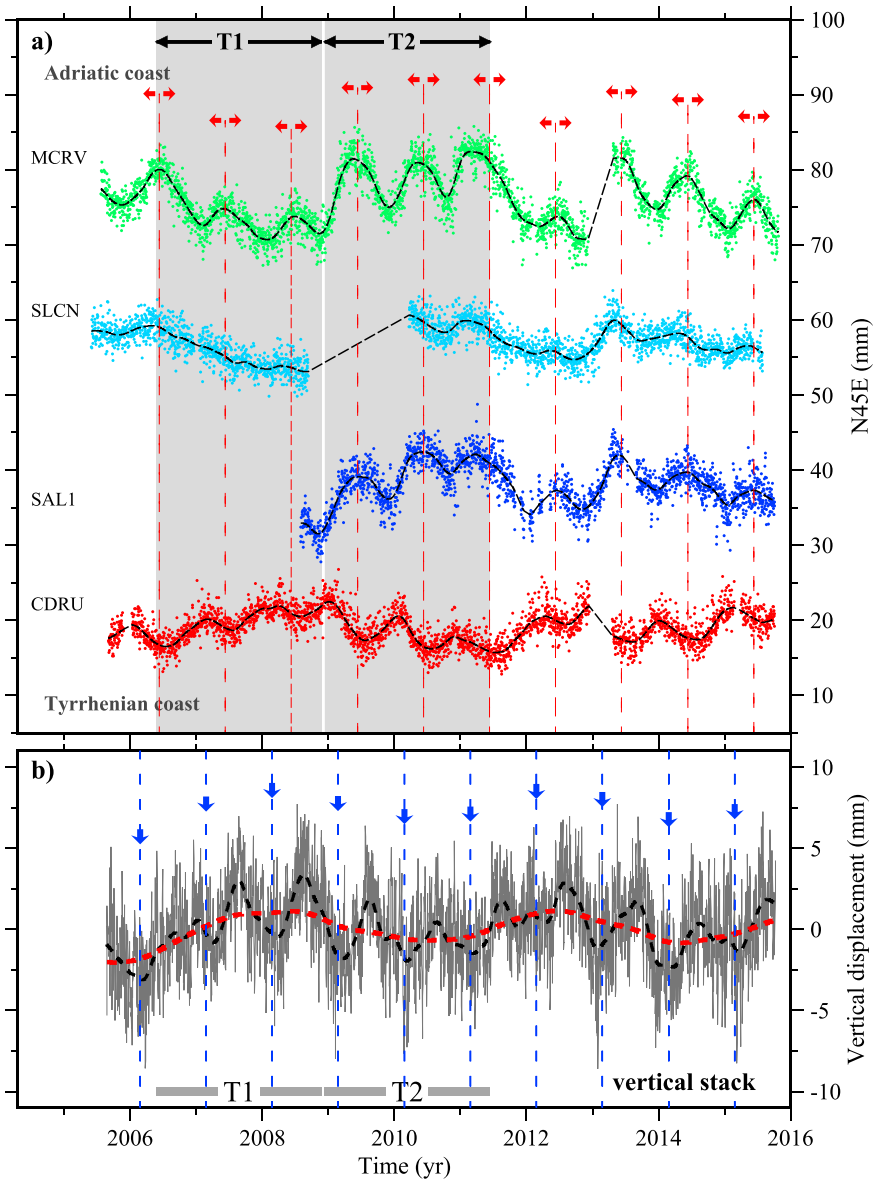

Figure 7. Comparison between the horizontal and vertical stack time series. (a) Detrended horizontal (N45E component) time series for selected sites in Figure 2 showing clear seasonal peaks. The red divergent arrows and dashed lines mark the average annual phase (0.44) of maximum positive horizontal dilatational strain (late spring). (b) Vertical stack time series (same as Figure 4c). The blue arrows and dashed lines mark the average annual phase (0.1) of maximum downward motion (winter).

are representative of the precipitation trend in the last decade in southern Apennines. Their positions are indicated in Figure 1, and their coordinates and main features are given in Table S2.

Rain gauge time series are shown in Figure 8 as monthly discrete values. We show also daily cumulative values and detrended daily cumulative series [*Roeloffs*, 2001] in order to accentuate the deviations relative to the 2003–2015 average trend. Maximum precipitations are generally concentrated in October–February showing significant interseasonal variability and a significant reduction in drought years 2007–2008 and 2012. The previously defined T1 and T2 intervals (see section 2) correspond to periods of anomalously low (T1) or high (T2) precipitations, followed by a significantly dry season in 2012.

3.2. Karst Spring Discharge

Further evidence of interannual hydrological variability is also visible in the discharge time series of large karst springs in the Apennines [*Fiorillo et al.*, 2015b].

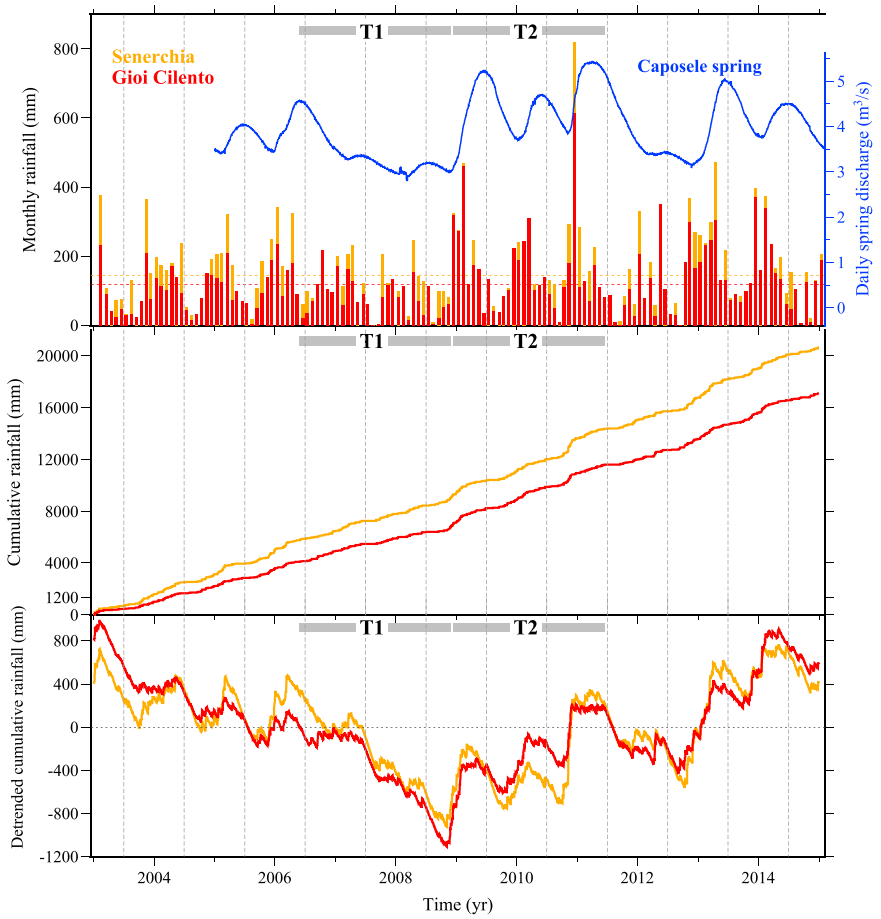

Figure 8. (top) Rainfall records at Gioi Cilento (red) and Senerchia (orange) rain gauges shown as monthly values and (middle) daily cumulative and (bottom) detrended cumulative time series. The orange/red horizontal dashed lines (Figure 8, top) depict the mean monthly cumulative values indicated in Table S2. In the top plot the daily discharge time series of Caposele spring (blue curve) is superimposed to rainfall time series.

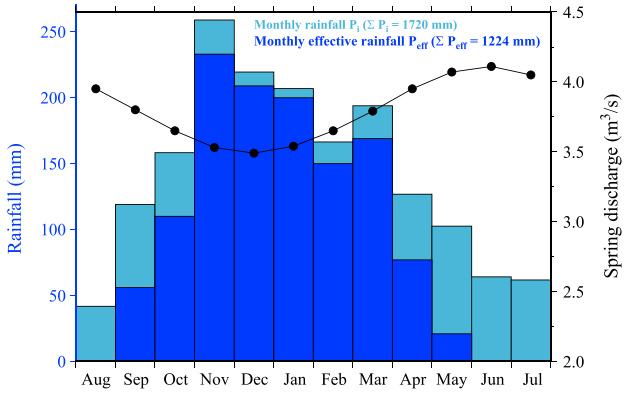

Figure 9. Comparison between the monthly mean rainfall values at Senerchia climate station and monthly mean discharge values at Caposele spring. The effective rainfall (P_{eff}) is defined as the difference between the monthly rainfall (P_i) and the evapotranspiration (E_p): $P_{eff} = P_i - E_p$. We compute the latter from temperature data by using the method by *Thornthwaite* [1948]. The recharge period generally starts in October, after the soil moisture capacity has been satisfied, and ends in May due to the increase of temperature and decrease of rainfall in spring–summer. The Caposele discharge has an almost opposite path, with minimum in December and maximum in late spring.

One of the largest karst springs of southern Italy is located near Caposele (Sorgente Sanità, 417 m above sea level (asl); spring location and catchment area in Figure 1). This spring is situated along the north-eastern boundary of the Picentini Mountains, it is primarily fed by the Cervialto massif [*Celico and Civita*, 1976] and it is characterized by a mean-annual discharge of about 4 m^3/s. Caposele is a basal spring, i.e., it drains directly the saturated zone of the aquifer, and it can be considered the only one draining Cervialto massif, since other springs have a considerable lower discharge [*Fiorillo et al.*, 2015a]. Besides, as no man-made modifications or groundwater pumping occurred in the spring catchment, this spring is strictly controlled by climate trends.

For these reasons the Caposele spring discharge can be assumed as a robust regional indicator for the state of recharge of the large karst aquifers in Southern Italy. The Aqueduct Company of Puglia (Acquedotto Pugliese S.p.A.) provided the daily discharge data for the Caposele spring for the period from January 2005 to October 2015 (Figures 4 and 8).

The maximum discharge at Caposele usually occurs in spring, some (4÷5) months after the period of maximum precipitation, whereas the minimum discharge takes place during the rainy months (Figure 8). This is shown in more detail in Figure 9, where we compare mean (over 2000–2015 interval) monthly values of total and effective (less the contribution of evapotranspiration) rainfall and spring discharge. The smooth shape of the hydrograph and its delayed response to rainfall indicate that the spring discharge is not affected by single events of rainfall, but it responds to the precipitation cumulated over several months [*Fiorillo and Doglioni*, 2010]. This behavior is mainly related to the prevalence of diffuse flow through fractures due to the coarse development and/or poor connection of the karst network [*Fiorillo*, 2009]. Indeed, the tectonic compressive phases of Miocene and the recent (since the Quaternary) evolution of internal Apennines areas, characterized by active crustal extension and regional uplift, have caused extensive block faulting, dropping of base levels, and, locally, the deposition of very thick continental depositional sequences between the carbonate ridges, hindering the development of a mature karst network [*D'Agostino et al.*, 2001; *Amoruso et al.*, 2013; *Fiorillo et al.*, 2015b]. Similarly to other aquifers in the Apennines [*Fiorillo et al.*, 2015b], this feature makes the wide karst systems of this area acting as large natural reservoirs of water with spring discharges reflecting both times of poor or abundant precipitation and climate changes occurring over long (years to decades) periods.

Both rainfall and spring discharge time series show variations in the annual signals. This is clear in the absence (e.g., during T1 period) of the characteristic increase of discharge at Caposele spring, usually observed during years with more abundant precipitation (e.g., T2 period) (Figure 8).

3.3. GRACE Data (Gravity Recovery and Climate Experiment)

The Gravity Recovery and Climate Experiment (GRACE), launched in March 2002, provides monthly measurements of the Earth's gravity field [*Tapley et al.*, 2004]. Taking into account the atmospheric circulation, the changes in the gravity field over the continent are mainly attributed [*Wahr et al.*, 1998] to variations in terrestrial water storage (TWS), which is a vertically integrated measure of water storage including groundwater, soil moisture, surface water, snow water, and vegetation water. Other mass changes in the study area, such as glacial isostatic adjustment and ice loss, are not significant or of much lower magnitude in the study area [*Boy and Lyard*, 2008]. GRACE gravity data can be therefore used to infer temporal variations in TWS and to estimate the response of the solid Earth to such loading.

Monthly measurements of the Earth's gravity field are usually translated into mass in units of equivalent water height (EWH). In this work we use the estimates of EWH obtained from the land monthly mass grids (GRCTellus Land [*Swenson*, 2012] available at http://grace.jpl.nasa.gov), which are calculated from the RL05 spherical harmonic solution and distributed with the support by the NASA Making Earth Science Data Records for Use in Research Environments (MEaSUREs) Program. We consider three solutions from different processing centers of the official GRACE Science Data System: JPL (Jet Propulsion Laboratory; RL05.DSTvSCS1411 solution [*Watkins and Yuan*, 2012]), GFZ (GeoforschungsZentrum Potsdam; RL05.DSTvSCS1409 solution [*Dahle et al.*, 2012]), and CRS (Center for Space Research at University of Texas, Austin; RL05.DSTvSCS1409 solution [*Bettadpur*, 2012]). All GRCTellus Land solutions use a Gaussian smoothing function with a 300 km half width [*Swenson*, 2012] to suppress errors at short spatial wavelengths [*Wahr et al.*, 1998]. We extract and calculate the average values for each of the three solutions from the monthly mass grids within 400 km from the point (15.6°E, 40.5°N). Following *Landerer and Swenson* [2012], we take into account data covariance between nearby grid points [*Swenson and Wahr*, 2006] to estimate TWS uncertainties using decorrelation lengths of 300 and 100 km for measurement and leakage errors, respectively. The solutions from the three data centers are represented in Figure S1 from April 2002 to April 2015 as anomalies with respect to the 2004–2010 average. The three time series are in very good agreement between ~2004 and 2011, whereas they are more scattered in the remaining time. This is probably due to the presence of more data gaps before the year 2003, when the satellites were not yet fully operational, and after 2011, when active "battery management" of GRACE satellites started [*Jean et al.*, 2015]. In order to improve the results, we generated a combined solution (Figure S1) by calculating the arithmetic mean of the three time series, as suggested by *Sakumura et al.* [2014] and *Jean et al.* [2015].

The 300 km resolution of the GRACE solution does not allow us to spatially define the spatial distribution of mass variability at the scale of the study area, and it is likely that the contribution from adjacent areas leaks

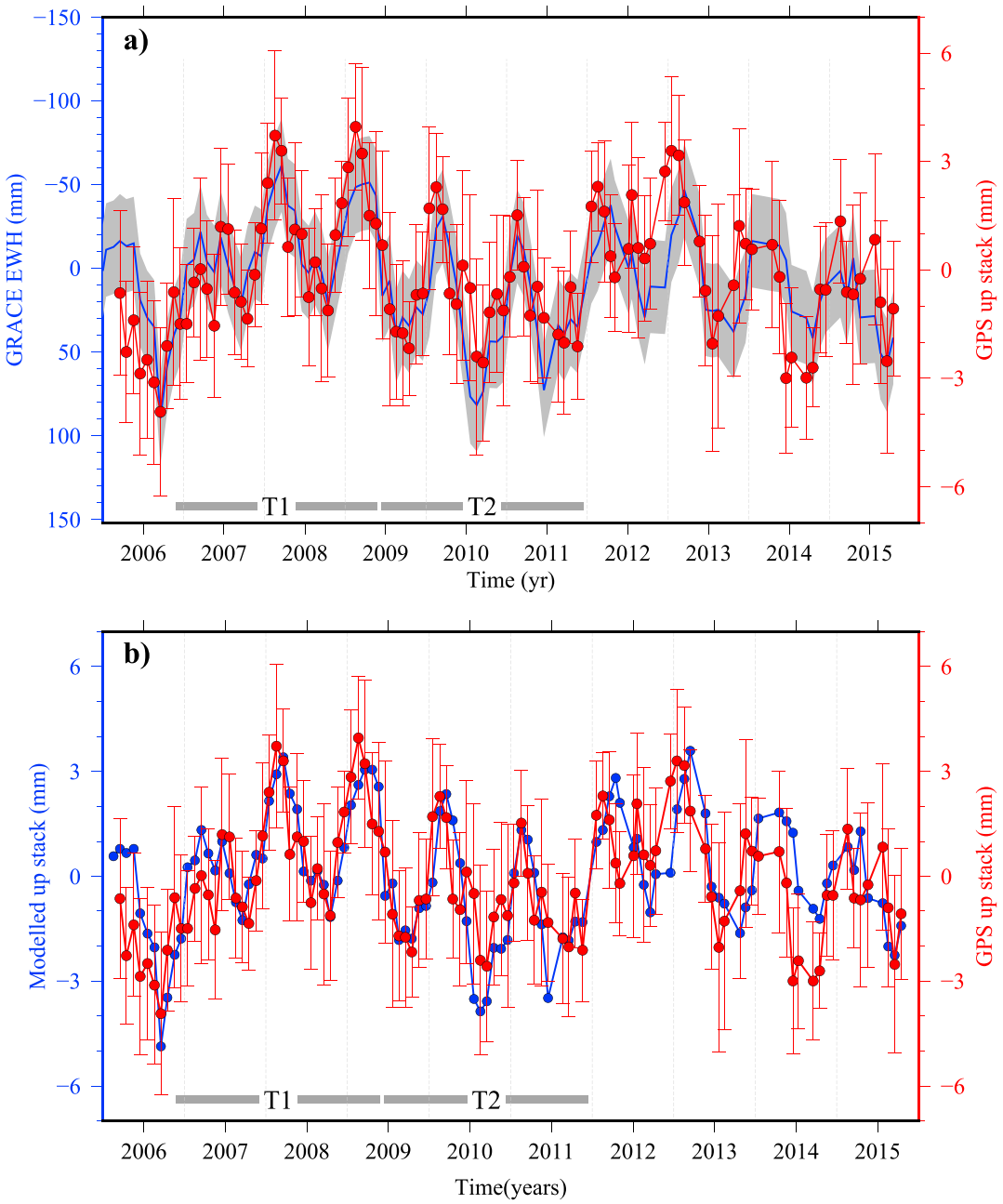

Figure 10. (a) Comparison between monthly equivalent water height GRACE data (blue line ± 1σ uncertainty) and stacked vertical GPS displacements sampled and averaged at the same epochs (red circles ± 1σ uncertainty). Notice the inverted vertical axis for the GRACE plot. (b) Comparison between the vertical modeled monthly time series induced by the GRACE EWH distribution (blue circles, see text for details) and the observed GPS time series (same as Figure 10a).

into our estimate of EWH. The 300 km scale is in fact large enough for GRACE mass solution being an average of TWS in the Apennines and in the nearby regions [*Wahr et al.*, 1998]. This kind of data therefore provides information about the influence of the temporal variability of the TWS on the observed GPS signal.

GRACE TWS time series, represented in Figures 10a (notice the reverse scale for GRACE data) and S1, show that higher annual TWS values generally occur in December–February. The drought years previously evidenced in rainfall and spring discharge time series (i.e., 2007–2008 and 2012) have lower TWS peaks in winter months with respect to the long-term average. T1 and T2 intervals correspond to TWS values which are, respectively, significantly below and above the 2002–2015 average and, consistently with rainfall and spring discharge data, indicate a significant multi-year variation of surface water and groundwater storage.

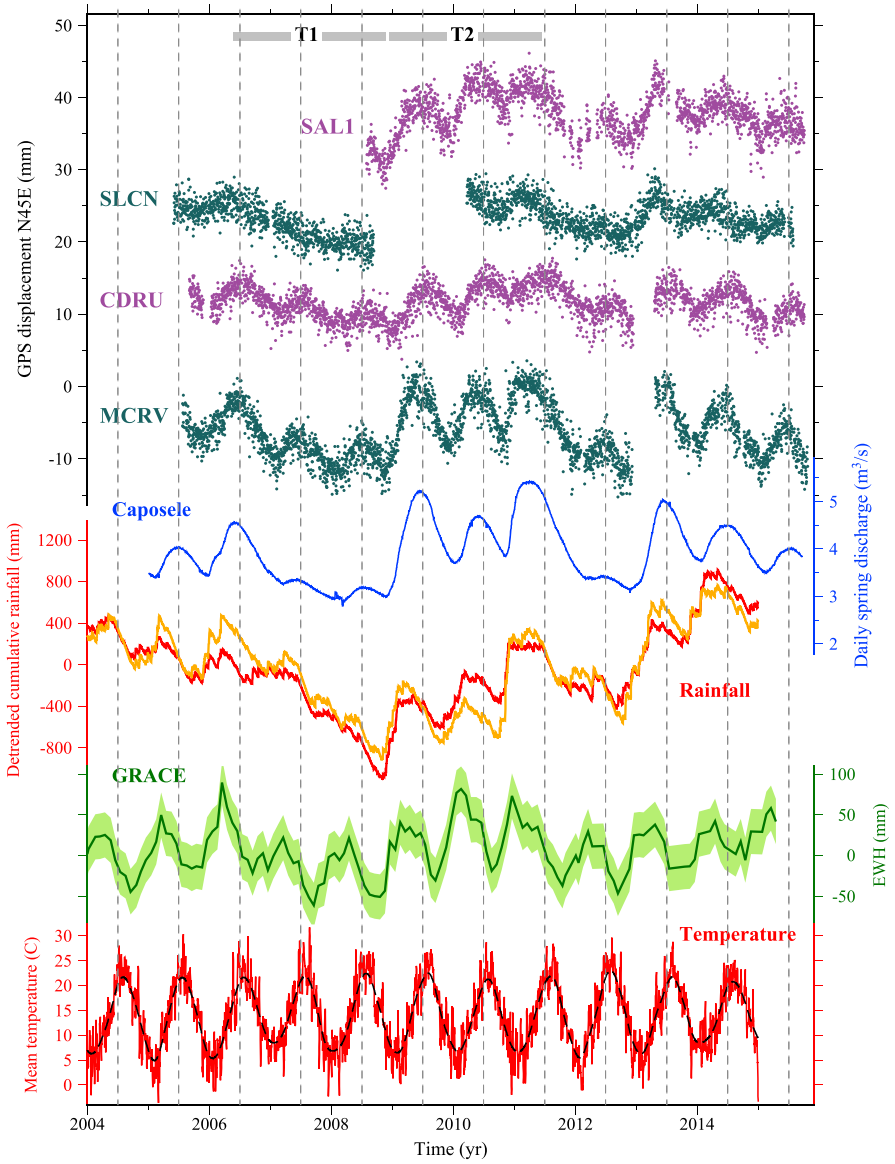

Figure 11. Comparison between GPS time series and hydrological records (i.e., rainfall, spring discharge, equivalent water height GRACE, and temperature data). GPS time series (grey and magenta dots) are the detrended horizontal component along direction N45E at selected sites in the dashed orange rectangle of Figure 1. Note that vertical axis for CDRU is inverted for clarity. Daily precipitation data at Gioi Cilento (red line) and Senerchia (orange line) rain gauges are represented as detrended cumulative rainfall. The blue line shows daily discharge data of Caposele spring. Monthly data of equivalent water height from GRACE satellites represent an average over the area under examination (green line $\pm 1\sigma$ uncertainty). The dark red and dashed black lines represent, respectively, the mean daily temperature values at Senerchia rain gauge and the 6 month Gaussian-filtered data.

3.4. Analysis and Correlation of Hydrological Time Series

As previously shown in section 3.2, we observe a systematic shift of several months between rainfall, with maximum values in autumn-winter, and the discharge of Caposele spring, which shows positive peaks in spring (Figures 8, 9, and 11). In karst aquifers, once the percolating water reaches the saturated zone, the pressure pulse is forced through phreatic conduits and almost instantaneously influences the spring discharge [*Ford and Williams*, 2007]. The time lag between recharge and discharge is therefore influenced by the duration of the water percolation through the vadose zone of the aquifer [*Fiorillo and Doglioni*, 2010]. Further factors can influence the time lag between recharge and discharge such as the time shift between snowfalls and snow melting, the presence of a cover made of pyroclastic deposits [*Fiorillo and Doglioni*, 2010], the spring catchment area [*Fiorillo et al.*, 2015b], and the eventual presence of low-permeability barriers, such as faults, which

compartmentalize the aquifers [e.g., *Celico et al.*, 2006]. Simple models of water circulation in unconfined karst aquifers relate the variations of the spring discharge to the elevation of the water table [*Manga*, 1999; *Fiorillo*, 2011; *Amoruso et al.*, 2013]. A high level of the basal spring discharge is associated with an increase of the hydrostatic pressure in the basal, saturated part of the aquifer. In particular, the variation of the water table height (Δh) causes a direct variation of the hydrostatic pressure: $\Delta P = \rho_w g \Delta h$ (ρ_w is water density, and g is gravitational acceleration) [e.g., *Miller*, 2008]. Aquifers held in carbonate rocks can experience seasonal fluctuations of the water table height of considerable magnitude, reaching several tens of meters [e.g., *LeGrand and Stringfield*, 1971; *Bella et al.*, 1998; *Miller*, 2008].

The seasonal fluctuations of TWS data measured by the GRACE satellites, showing "positive" peaks (i.e., higher values of equivalent water height) in fall-winter, appears to be roughly simultaneous to rainfall and, accordingly, to precede the positive spring discharge peaks of some months (Figure 11). We can therefore recognize two main seasonal hydrological stages separated by 5–6 months which, as will be shown in the following sections, correlate with specific features in the GPS time series. The first hydrological stage, occurring in late fall/winter corresponds with the peak of the rainy season and maximum snow coverage at high elevation. This stage likely corresponds to the maximum overall hydrological loading as suggested by peaks in EWH measured by GRACE. The second episode corresponds to the peak discharge from karst springs occurring in late spring (as shown by the positive peak of the Caposele discharge in Figure 8). This second stage likely reflects the infiltration of water within the karst system and corresponds to maximum value of hydrostatic pore pressure within the saturated part of the karst aquifers. The occurrence of single (i.e., 2012) or repeated (2007–2008) years with scarce precipitations are clearly reflected in the absence of the characteristic smoothed peak in spring discharge time series (Figure 8) and control the occurrence of drought events [e.g., *Fiorillo*, 2009, 2013].

4. Comparison and Main Features of GPS and Hydrological Time Series

GPS horizontal time series at stations close to the karst aquifers appear to be highly correlated with the discharge of the Caposele spring (Figure 11). Cross-correlation analysis (Figure 12) indeed demonstrates that high (0.89) correlation is observed not only at the local scale, i.e., between Caposele spring discharge and the near (∼6 km far) GPS station MCRV, but also between the spring discharge and displacement time series at farther (∼40 km) sites such as SAL1 and CDRU (respectively, 0.77 and 0.72). In particular, the dilatation strain, calculated in a polygon defined by stations located at a distance between 36 and 58 km from the spring, is highly correlated (correlation = 0.6) with the Caposele discharge time series (Figure 4). These observations confirm the regional nature of the multiyear discharge observed at the Caposele spring and indicate that negative precipitation trends and aquifer exhaustion are associated with reduced or negative dilatational strain (T1), whereas episodes of increasing rainfall (aquifer recharge) are associated with sustained dilatation (T2) (Figures 4 and 11).

High cross-correlations between horizontal displacements and spring discharge are associated with lag times of ±0–2 months (Figures 11 and 12), indicating minor temporal variability of the ground deformation associated with spring discharge.

Vertical displacements appear to be preferentially correlated with GRACE TWS data, showing subsidence in high water storage periods (autumn-winter) and uplift in summer. In order to compare vertical GPS displacements and GRACE TWS data at the same temporal resolution, we compute monthly averages of the daily vertical GPS stacked position centered on the date of GRACE acquisitions estimating the uncertainty from the standard deviation of the monthly average (Figure 10a). We observe that the two sets of measurements present a remarkable (0.71) inverse correlation with a limited time lag (GPS vertical stack precedes GRACE of 0–1 month). The worse correlation in the last ∼4 years is probably related to the decreasing GRACE data quality after 2011 [*Jean et al.*, 2015], as we discussed in section 3.3. At the multiyear scale, subsequent years of low TWS (e.g., 2007–2008 and 2012–2013) are associated with a general motion of uplift involving the whole studied area (Figure 10a). Further details about the cross-correlation analysis are given in the supporting information.

We suggest that (i) two main processes are responsible for the observed deformations and that (ii) different spatial and temporal patterns allows us to observe their separated effects in the horizontal and vertical components. The significant correlation with spring discharge and the spatial link with karst areas suggests that

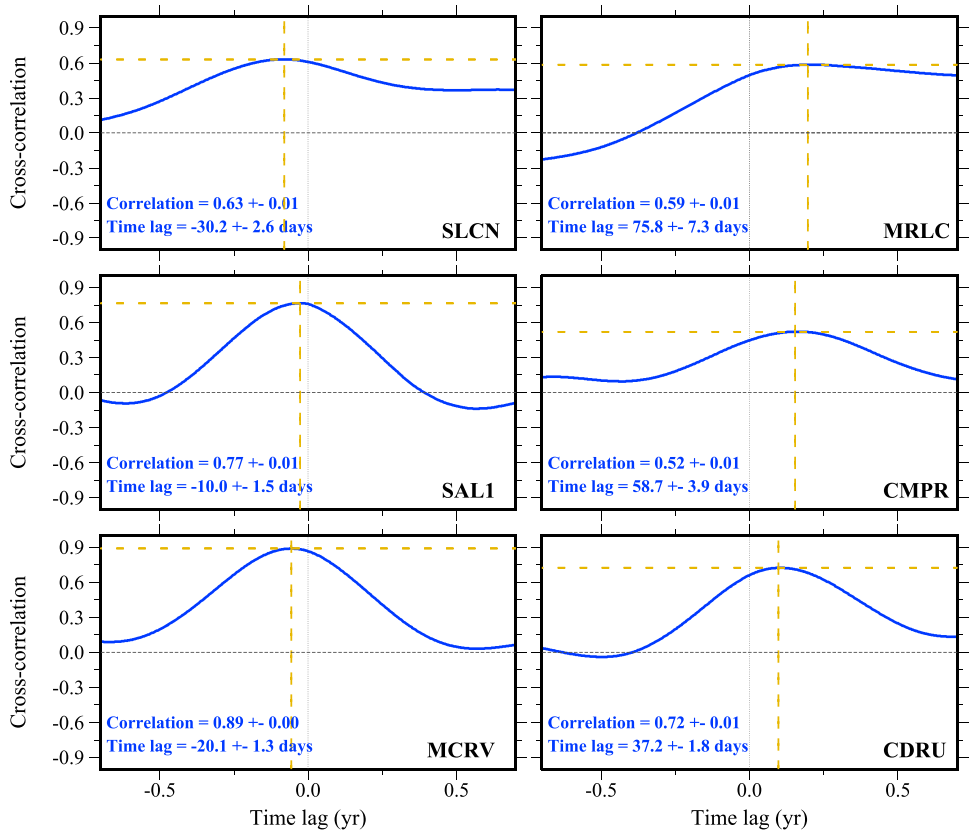

Figure 12. Plots of cross correlation between the observed N45E component and daily spring discharge for selected GPS sites. The horizontal axis indicates the temporal shift of the observed deformation with respect to spring discharge. The vertical axis indicates the value of correlation at different time lags. Horizontal and vertical dashed yellow lines pick the maximum value of correlation and the corresponding amount of time lag, whose values are printed in the left corner together with 1σ uncertainties estimated through the bootstrap method [*Moore et al.*, 2003] (see supporting information for further details).

the observed horizontal deformation depends, on the first order, on a mechanical process sensitive to variations of hydrostatic pressure beneath karst aquifers, which induces time-dependent opening of fractures in the shallow crust (see discussion in the next section). The high correlation with GRACE TWS suggests that, similarly to other regions [e.g., *Borsa et al.*, 2014], the vertical component mainly reflects the elastic response of the solid Earth to variations of TWS.

5. Discussion

5.1. Elastic Response to Hydrological Loading

We suggest that the behavior of the vertical GPS component is consistent with the elastic response to loading at both seasonal and multiyear scales. Here we test which amount of the observed geodetic signal could be explained as the elastic response to the variations of GRACE TWS loading. To this aim, we calculate the surface deformation induced by the EWH variations recorded by GRACE satellites. We carry out the modeling by using the REAR (Regional ElAstic Rebound calculator) code [*Melini D. et al.*, 2014], which computes the response of a solid, nonrotating, elastic, isotropic Earth to assigned surface load variations. In a first step REAR computes the response to a finite-sized disc load of unitary thickness with a Heaviside load history. The set of implemented Love numbers have been calculated by *Melini D. et al.* [2014] using the seismological model STW105 [*Kustowski et al.*, 2007], which is an update version of the Preliminary Reference Earth Model (PREM) [*Dziewonski and Anderson*, 1981] obtained by replacing the top three kilometers of oceanic water with underneath rock material. In a second stage, by using the principle of superposition, REAR combines the previously calculated Green functions to estimate the horizontal and vertical displacements caused by the imposed load model. The load model is constructed, in each time frame, by discretizing the gridded GRACE EWH values in disc-shaped elements (25 km radius).

Following the same procedure used to calculate the observed vertical stack, the predicted displacement shown in Figure 10b is the stack of the displacements calculated at the same 18 stations. The results (Figure 10b) show that the vertical deformation induced by the EWH load distribution over an area within a range of ≈1000 km from the observation point produces a remarkable fit, reproducing both the observed amplitude and the multiyear trend. This suggests that, as observed elsewhere [e.g., *Borsa et al.*, 2014; *Chanard et al.*, 2014], the observed vertical displacement is significantly controlled by the elastic response of the lithosphere to the hydrological loading. The percentage of RMS reduction [e.g., *Fu et al.*, 2015] (∼43%) obtained by subtracting the GRACE-derived displacement from GPS time series in the best fit 2006–2010 interval suggests that a significant part of the vertical signal is dominated by the elastic response of the solid Earth to the surface water loads detected by GRACE.

The elastic response of the crust to a surface load is characterized by a ratio between vertical and horizontal components of about 2–3 for a concentrated load and much larger if the load is spatially distributed [*Wahr et al.*, 2013]. The calculated horizontal displacements obtained by the TWS GRACE loading model reach maximum amplitudes of about 1 mm; i.e., they are 1 order of magnitude smaller than the maximum oscillations (∼1 cm) observed at MCRV, MRLC, SAL1, and SLCN and do not reproduce the sign and rapid spatial variations of the horizontal motion around the karst aquifers of the Apennines. The limited resolution of GRACE does not allow to define the spatial distribution of the TWS loading at the scale of the Apennines and in particular to test if the karst aquifers are the main sources of TWS loading. However, even in the case of localized load due to the karst aquifers, the elastic response to loading could not explain the observed horizontal signal. In this case, in fact, the predicted elastic horizontal motions would be directed toward the hydrologic loading source, whereas the opposite would occur when the load is removed (horizontal motion away from the source). This is the opposite to what is observed around the karst aquifers where seasonal and multiyear episodes of divergence are observed in combination with increasing water loading (e.g., interval T2), and shortening episodes are observed with decreasing water loading (e.g., interval T1) (Figures 3 and 4). We thus suggest that the elastic response to TWS does not explain the localized observed horizontal transient signals, and therefore, another mechanism is required.

5.2. Response of an Anisotropically Fractured Crust to Variable Hydrostatic Pressure

The analyses presented in the previous sections show that transient deformations in the horizontal components are distinctly correlated to the variations of spring discharge from karst aquifers but their pattern cannot be reproduced by the elastic response of the solid Earth to surface loading. Simple hydrogeological assumptions (section 3.4) allows us to assimilate the spring discharge variations to the hydrostatic pressure variations inside the aquifer. We identify two processes which are specifically sensitive to changes of hydrostatic pore pressure in the shallow crust and potentially able to reproduce the observed horizontal deformation. Increasing pore pressure reduces the effective normal stress and facilitates slip on shear dislocations if the stress conditions satisfy failure criteria for preexisting surfaces. Alternatively, variable hydrostatic pore pressure controlled by the variation of the water table height may control the opening of conductive, interconnected water-filled fractures within an unconfined aquifer in the shallow crust. The main difference between these two processes, which can be used as a diagnostic feature, is the capability to produce opposite directions of displacement under stress variations associated with changes of pore pressure. Whereas tensile fracture opening is a reversible process under pore pressure variations (i.e., when pore pressure returns to its initial level the fracture aperture returns to its initial state), a pore pressure decrease does not produce an inversion of slip direction on a shear dislocation. The first mechanism (slip on a shear dislocation) would, thus, implicate a monotonic direction of the transient deformation (as observed in slow slip events on subduction zones); i.e., the transient motion would be systematically directed toward the Tyrrhenian or the Adriatic coast for stations located on the opposite side of the symmetry axis observed in Figure 2. We observe instead an alternating dilatation/contraction deformation (Figures 3 and 4), which appears more consistent with an opening fracture mechanism.

Nearly isotropic episodes of expansion/contraction are usually observed in alluvial poorly consolidated materials where variations of the water table correspond to isotropic deformation [e.g., *Hoffmann et al.*, 2001; *Preisig et al.*, 2014]. The pattern and magnitude of the observed deformation require, on the other hand, a process able to produce an anisotropic horizontal deformation with a preferential NE-SW expansion direction and a significantly smaller vertical deformation.

Anisotropy in the shallow crust can be caused by preferentially aligned fractures and microcracks [e.g., *Amadei*, 1996; *Pastori et al.*, 2009]. We thus ascribe the observed horizontal signal to the response of ~N140, subvertical, fluid-filled, conductive system of fractures to variations of the water table height. Following that logic, the observed displacements are the result of dilatation/contraction of the fluid saturated anisotropic media in response to variations of the hydrostatic pressure in the karst aquifer.

Hydrogeological [*Calcaterra et al.*, 1994; *Celico et al.*, 1994; *Del Prete et al.*, 2007] and seismological [*Pastori et al.*, 2009] observations show that the shallow crust in the southern Apennines is characterized by a primary fracture pattern oriented in NW-SE direction. Detailed information (fracture spacing, dimension, aperture, and penetration depth) about the spatial distribution and mechanical characteristic of this media is not accessible at the spatial scales of the examined area. We therefore simulate the response of an horizontally anisotropic poroelastic aquifer to variations of the water pressure by using a simple model constituted by vertical tensile dislocations embedded in an elastic half space. We constrain the time-dependent opening of these dislocations to be linearly related to the discharge of the Caposele spring, whose time variations are considered to closely reflect the regional hydrological signal [*Fiorillo*, 2009].

The main simplifying assumptions implied in this model are (i) linear relation between the water pressure variation and the observed displacement and (ii) equilibrium condition for poroelastic deformation reached instantaneously whenever the pore pressure changes occur. The last assumption implies that the diffusion of pore pressure variations inside the aquifer is a relatively fast process so that the coupling between pore pressures and stresses in the skeleton matrix is instantaneous. The cumulative effect of a group of small tensile fractures embedded in a fractured region is, at a certain distance, roughly equivalent to the one caused by a single tensile dislocation, with ad hoc parameters, located inside the region [*Maccaferri*, 2010]. Since most of the observations (GPS stations) lie at the boundaries or just outside of the carbonate massifs (Figure 3), we model the first-order features of the signal using single tensile dislocations roughly located beneath the main karst aquifers. We employ three vertical tensile dislocations buried in an homogeneous elastic medium [*Okada*, 1985] with Poisson's ratio of 0.25, whose geometries reproduce the observed velocity deviations relative to the long-term trend (Figure 3). The dislocations are located approximately along the symmetry axis of the horizontal deformation, and we select their positions and lengths (Figure 3) in order to reproduce the horizontal divergence across the three main karst systems of the southern Apennnines: (1) Cervialto and Polveracchio-Raione massifs (near MCRV site), (2) Marzano-Ogna Mounts massif (near MRLC), and (3) Alburni, Motola, and Cervati massifs (near CDRU, CMPR, SAL1, SLCN, MTSN, and MCEL). The strike angle for all the three dislocations is 140°, consistently with the observed orientation of the primary fracture pattern [*Calcaterra et al.*, 1994; *Celico et al.*, 1994; *Del Prete et al.*, 2007; *Pastori et al.*, 2009]. We fix the depth of the top edge of the dislocations at 100 m, since small variations of this parameter only affects the deformation in the very near field.

The opening of water-filled fractures in the phreatic zone is due to the variation of the hydrostatic pressure, which is in turn related to the variation of the height of the water table. By assuming linearity between the water table height variation and the rate of spring discharge, we impose a homogeneous time-dependent opening of the three dislocations ($A(t)$) by scaling it to the discharge of Caposele spring (Figure 4), taken as a proxy for the regional elevation of the groundwater table within the carbonate aquifers. For this purpose we use the following relation:

$$A(t) = \frac{Q(t) - Q_{\min}}{Q_{\max} - Q_{\min}} A_{\max} \tag{1}$$

where $Q(t)$ is the Caposele discharge rate observed at time t and $Q_{\min}$ and $Q_{\max}$ are, respectively, the minimum and maximum Caposele spring discharges observed in the considered time interval (2005–2015). The dislocation opening therefore varies between 0, corresponding to the minimum value of spring discharge in the considered time interval (2005–2015), and a maximum value $A_{\max}$, in correspondence of the maximum value of spring discharge. An uniform opening is imposed over all the dislocation. We conduct a grid search by varying the opening parameter $A_{\max}$ between 1 and 200 mm and the vertical width of the dislocations between 0.1 and 8 km, and we minimize the fit to the detrended horizontal time series. We neglect the Earth surface curvature for a first-order estimate of the near-field effects and the exact topographic trend, considering the half-space surface as an average reference elevation above the sea level (≈600 m asl) [*Lisowski*, 2007]. The comparison between observed and predicted horizontal displacements (Figure 13) shows that this simple model

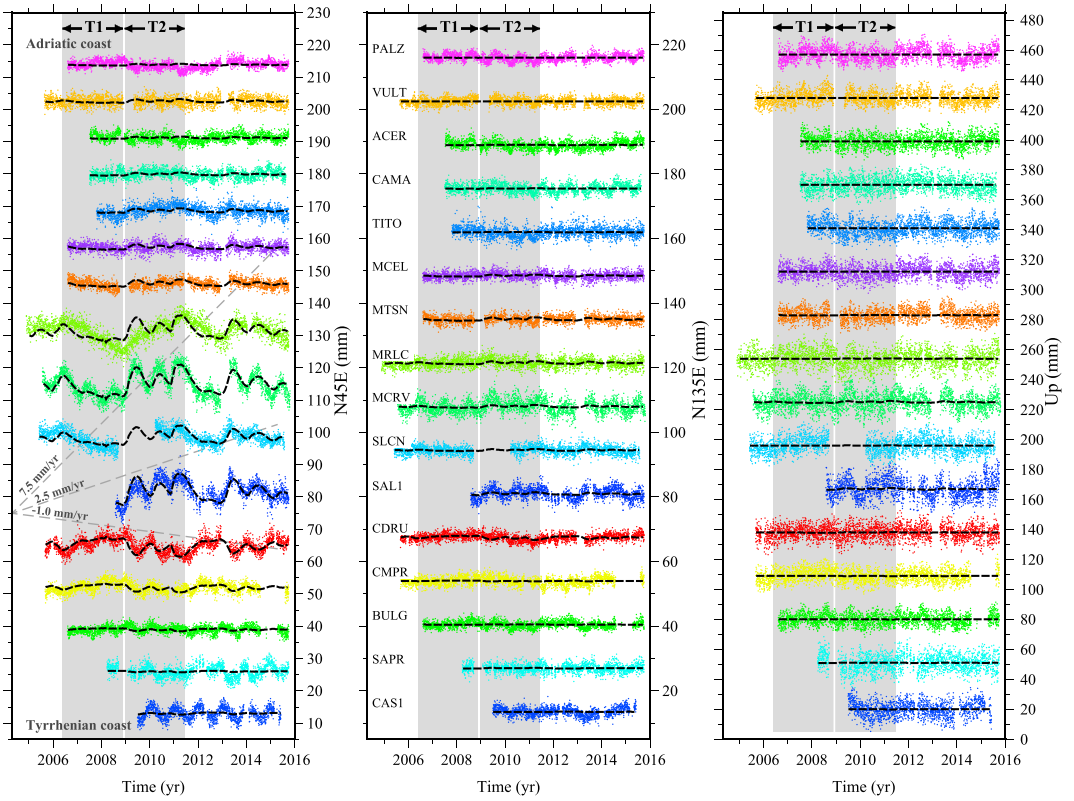

Figure 13. Same as in Figure 2 except that the long-term trend has been removed and the bold black dashed lines indicate the modeled time series obtained from the minimum RMSD model (corresponding to the blue cross in Figure 14).

reproduces to the first order the main features of the observed signal, including the limited deformation in the N135E and vertical components. The agreement in the horizontal components is particularly good (root mean square deviation (RMSD) $\leq$ 2 mm) not only at MCRV, located near Caposele spring, but also at farther sites such as CDRU, CMPR, MTSN, SAL1, and SLCN. The worse agreement occurs at MRLC (RMSD =2.5 mm), which shows reduced seasonal variations and an enhanced delay compared with the Caposele spring discharge. Figure 3 shows velocities calculated separately for T1 and T2 intervals using the best fit model. Since the vertical deformation related to a tensile dislocation decays quickly with the distance from the dislocation, the modeled vertical component is almost negligible at every site (Figure 13).

The minimum misfit corresponds to values of 60 mm and 1.5 km of maximum opening and tensile dislocation width, respectively (Figure 14), with a significant trade-off as a function of the investigated parameters and a large range of the acceptable values. The product of the two parameters ($\approx$90 m^2) along the valley of minimum misfit is, on the other hand, remarkably stable, especially for low values of the dislocation width. This product, when multiplied with the dislocation lengths, could provide a rough estimate of the maximum storage capacity variation available from the opening dislocations in the considered period. Considering the length of the tensile dislocation beneath the Picentini massif (15 km), the maximum storage capacity equals 1.35×10^6 m^3 (15 km $\times$ 90 m^2) which is $\approx$1% of the average annual discharge of the Caposele spring ($\approx 124 \times 10^6$ m^3).

Many important physical aspects are neglected in our simple modeling approach such as a realistic characterization and geometry of the fractured medium, a reliable range of the hydrostatic pressure variations, and the depth dependency fracture opening. The main objective of the modeling is, on the other hand, to verify a first-order linear dependency of the observed, sustained episodes of anisotropic divergence/shortening in the karst aquifers on the hydrostatic pore pressure variations as measured by spring discharge.

5.3. Thermoelastic Strain

In areas where the topographic relief is not negligible, the thermoelastic strain due to surface temperature variations can be an important cause of deformation [*Ben-Zion and Leary*, 1986; *Prawirodirdjo et al.*, 2006;

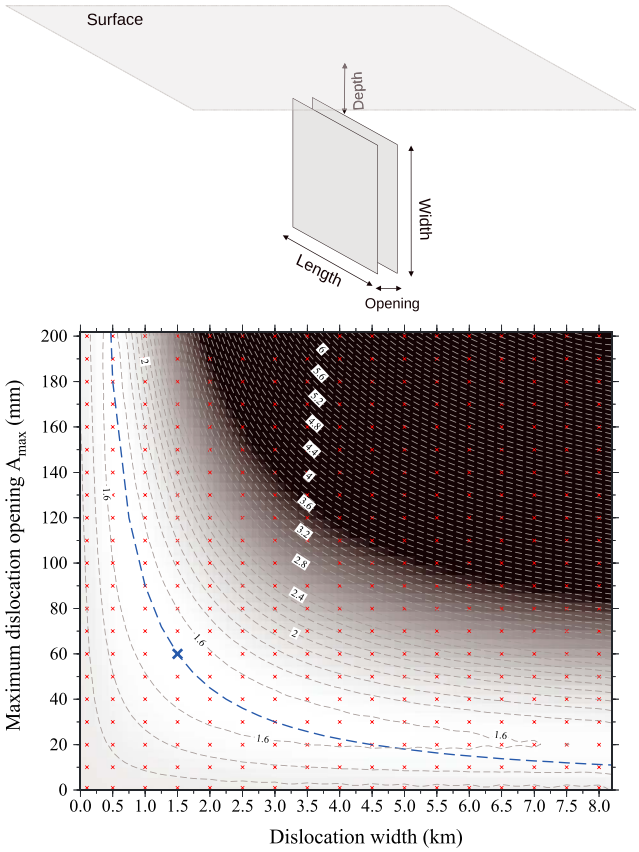

Figure 14. (top) Schematic representation of the model geometry. (bottom) RMS deviation between the observed and modeled horizontal time series for different values of width and maximum opening of the tensile dislocations. Red crosses indicate model realizations, and the grey dashed contours are interpolated between those points and plotted at 0.1 mm intervals. The blue cross indicates the minimum RMSD model. The blue dashed line indicates the parameters values whose product is constant and equal to the best fit 1 (60 mm × 1.5 km). The color scale is saturated at 4 mm.

Ben-Zion and Allam, 2013]. Although recent studies limited the role (no more than 25%) of the thermoelastic strain in controlling seasonal signal [*Tsai*, 2011; *Ouellette et al.*, 2013], its importance cannot be completely ruled out [*Dong et al.*, 2002].

The temperature data of the area under study (Senerchia site; Figure 11) show that the differences of the peak-to-peak amplitudes between dry (e.g., 2007–2008) and wet (e.g., 2009–2011) years amount to few degrees (≈3°C). Since the thermoelastic strain is linearly related to the peak-to-peak temperature amplitude [*Ben-Zion and Leary*, 1986; *Tsai*, 2011], these differences could not explain the variation of the deformation between dry and wet years (up to 1 cm; e.g., Figure 11). This is especially visible in the dry year 2012, when no noticeable change in peak-to-peak temperature amplitude are recorded compared to wet years (Figure 11), in spite of high variations of the observed displacement (Figure 11). Furthermore, the positive (i.e., expansion) peaks at MCRV site, which is a few kilometers far from Senerchia site (≈6 km), occurring in spring, anticipate the summer temperature peaks (Figure 11). This temporal shift is in the opposite sense compared to the typical temperature-deformation temporal sequence which characterizes the thermoelastic strain [*Ben-Zion and Leary*, 1986].

Tsai [2011] computed the equations of the displacement generated by the response of an elastic half space to sinusoidal (both in time and in space) surface forcing due to atmospheric temperature variations. The effect of a thin unconsolidated layer cover is also taken into account. By using the equations (11a) and (11b) of *Tsai* [2011], we estimate the expected horizontal and vertical surface displacements due to high end surface temperature variations. We assume peak-to-peak temperature variations $\Delta T = 40$°C, wavelength of the spatial temperature variation $\lambda = 20$ km on the basis of the local topography [*Ben-Zion and Leary*, 1986], annual period ($\omega = 2 \cdot 10^{-7}$ s^{-1}), varying values of the upper layer thickness (0–5 m) and typical values of Poisson's

ratio (0.25), coefficient of linear thermal expansion (10^{-5}°C^{-1}), and thermal diffusivity coefficient (10^{-6} m^2/s) [*Ben-Zion and Leary*, 1986; *Prawirodirdjo et al.*, 2006; *Tsai*, 2011; *Ben-Zion and Allam*, 2013]. The maximum peak-to-peak amplitude of the horizontal displacement obtained in this way amounts to about 2 mm.

Given these observations, we expect that the thermoelastic strain is not able to explain the majority of the observed GPS horizontal deformation. In particular, it could not recover the outstanding multiyear variation observed in the horizontal time series, especially at sites with small annual signal and high multiyear variations, e.g., MRLC site (Figure 2).

As for the vertical displacement, the amplitude estimated by using the equations of *Tsai* [2011] is <1 mm. Nevertheless, the magnitude of the vertical deformation would be increased by about a factor of 3 at the near surface if GPS stations are anchored within the thermal boundary layer [*Tsai*, 2011]. The thermoelastic strain could therefore give some contribution to the observed displacement at some sites inducing local variations of the vertical amplitude, especially at the annual temporal scale.

6. Conclusions

The primary result of this study is that horizontal and vertical geodetic time series may reflect different hydrological processes. Transient deformation signals in the horizontal time series reveal a currently underappreciated source of large-scale transient signals: the deformation of karst aquifers induced by variations of the water table and resulting hydrostatic pressure variations. We suggest that the main mechanism controlling the observed horizontal transient signal is the effect of time-dependent hydrostatic pressure on fluid-filled, conductive fracture systems beneath large karst aquifers. The simple first-order approach used to model the observed transient signal (single tensile dislocations beneath the main karst systems) reflects the current limited knowledge of the large-scale mechanical properties (fracture densities, rheology, and poroelastic parameters) of the karst systems but shows a remarkable first-order agreement between the model and the observations (Figure 13). The depth extent in the crust of this deformation source is not well resolved with available data and knowledge. Previous studies about karst regions have pointed out the transient water flow in the vadose zone after heavy rainfalls as the source of the observed deformation. Our work, however, shows that the deformation is significantly delayed with respect to rainfall and clearly correlated with variations of the basal spring discharge. This points out the variations in the water level of the phreatic (saturated) zone as the source of deformation. These differences in the observed deformation could be ascribed to the different development of the karst circulation and the degree of tectonic fracturing among various karst regions. Resolving more accurately the depth parameter, however, have significant implications for the understanding of the time-dependent permeability of the shallow crust [*Ingebritsen and Gleeson*, 2015] of the penetration of meteoric waters in the ductile regime [*Menzies et al.*, 2014] and of the role of fluid pressure variations on seismic rupture nucleation/triggering phenomena at seismogenic depths [*Miller*, 2008].

As the phases of recharge and discharge of the karst aquifers of the Apennines (and in the Mediterranean region in general) are influenced by climatic factors (Northern Atlantic Oscillation), we highlight a connection between large-scale climatic patterns and transient deformations of the shallow crust.

The vertical time series can be satisfactorily reproduced by modeling the deformation induced by the surface water loads estimated from the GRACE satellites data. The percentage of RMS reduction is ~43% when we subtract GRACE-derived displacement from GPS results in the best fit 2006–2010 interval, suggesting that a significant part of the vertical signal is dominated by the elastic response of the solid Earth to surface water loads detected by GRACE.

Parsing out the contribution of hydrological processes on geodetic measurements is an important task with significant implications for the accurate estimation of tectonic deformation. Our results show that, since 2005, two complete ~4 year cycles of hydrologically related episodes of deviations from decadal horizontal strain rate (Figure 6a) and vertical displacements (Figure 6c) have occurred. Sustained multiyear vertical velocity (±1 mm/yr) and horizontal strain rate (±50 nstrain/year) deviations may thus significantly affect the trend estimates based on short time intervals, considering the similar magnitudes of the decadal trends.

The result of our work emphasizes the need to jointly consider both the horizontal and vertical components for the investigation of hydrologically induced deformations. Our study shows, in fact, that the different sensitivities of vertical and horizontal components produce a space-time separation of (1) the elastic response of solid Earth to surface water loads and of the (2) the anisotropic response of fractured karst aquifers to

variations of hydrostatic pore pressure. This spatiotemporal separation allows us to track with geodetic measurements the different phases of the water cycle in the southern Apennines: from maximum hydrological loading at the surface to maximum hydrostatic pressure beneath karst aquifers.

Acknowledgments
We thank the reviewers Don Argus, Bill Hammond, and the Associate Editor Emma Hill for careful reviews and insightful and detailed comments that significantly improved this manuscript. We also thank Elisabetta Preziosi, Kristel Chanard, Maria Elina Belardinelli, Eleonora Rivalta, and Philip England for helpful discussions. Figures have been produced by using Generic Mapping Tools (GMT) software [*Wessel and Smith*, 1998]. The RINEX daily files from RING GPS stations can be accessed at http://ring.gm.ingv.it, while the other GPS data can be obtained by contacting the corresponding senior author (nicola.dagostino@ingv.it). We thank Stefano Calcaterra (ISPRA) for the rinex data of CAMA GPS station. Rainfall and temperature data are provided by Protezione Civile Regione Campania (http://centrofunzionale.regione.campania.it/index.php/rete-di-monitoraggio), Caposele spring discharge data are provided by the Aqueduct Company of Puglia (Acquedotto Pugliese S.p.A.; g.ventafridda@aqp.it). GRACE satellites data have been downloaded from GRCTellus Land http://grace.jpl.nasa.gov.

References

Allocca, V., et al. (2007), *Illustrative Notes of the "Hydrogeological Map of Southern Italy"*, Istituto Poligrafico e Zecca dello Stato, Roma.

Allocca, V., F. Manna, and P. De Vita (2014), Estimating annual groundwater recharge coefficient for karst aquifers of the southern Apennines (Italy), *Hydrol. Earth Syst. Sci.*, *18*, 803–817, doi:10.5194/hess-18-803-2014.

Álvarez García, F. J., M. P. Lorente-Lorente, and M. J. OrtizBevia (2012), Quasi-quadrennial variability in European precipitation, *Int. J. Climatol.*, *32*, 1295–1309, doi:10.1002/joc.2351.

Amadei, B. (1996), Importance of anisotropy when estimating and measuring in situ stresses in rock, *Int. J. Rock Mech.*, *33*, 293–325, doi:10.1016/0148-9062(95)00062-3.

Amoruso, A., L. Crescentini, M. Petitta, and M. Tallini (2013), Parsimonious recharge/discharge modeling in carbonate fractured aquifers: The groundwater flow in the Gran Sasso aquifer (Central Italy), *J. Hydrol.*, *476*, 136–146, doi:10.1016/j.jhydrol.2012.10.026.

Amoruso, A., L. Crescentini, S. Martino, M. Petitta, and M. Tallini (2014), Correlation between groundwater flow and deformation in the fractured carbonate Gran Sasso aquifer (INFN underground laboratories, central Italy), *Water Resour. Res.*, *50*, 4858–4876, doi:10.1002/2013WR014491.

Amos, C. B., P. Audet, W. C. Hammond, R. Bürgmann, I. A. Johanson, and G. Blewitt (2014), Uplift and seismicity driven by groundwater depletion in central California, *Nature*, *509*, 483–486, doi:10.1038/nature13275.

Argus, D. F., Y. Fu, and F. W. Landerer (2014), Seasonal variation in total water storage in California inferred from GPS observations of vertical land motion, *Geophys. Res. Lett.*, *41*, 1971–1980, doi:10.1002/2014GL059570.

Avallone, A., et al. (2010), The RING network: Improvement of a GPS velocity field in the central Mediterranean, *Ann. Geophys.*, *53*(2), 39–54, doi:10.4401/ag-4549.

Bakalowicz, M. (2005), Karst groundwater: A challenge for new resources, *Hydrogeol. J.*, *13*(1), 148–160, doi:10.1007/s10040-004-0402-9.

Bar-Sever, Y. E., P. M. Kroger, and J. A. Borjesson (1998), Estimating horizontal gradients of tropospheric path delay with a single GPS receiver, *J. Geophys. Res.*, *103*(B3), 5019–5035, doi:10.1029/97JB03534.

Bella, F., P. F. Biagi, M. Caputo, E. Cozzi, G. Della Monica, A. Ermini, W. Plastino, and V. Sgrigna (1998), Aquifer-induced seismicity in the central Apennines (Italy), *Pure Appl. Geophys.*, *153*(1), 179–194, doi:10.1007/s000240050191.

Ben-Zion, Y., and P. Leary (1986), Thermoelastic strain in a half space covered by unconsolidated material, *Bull. Seismol. Soc. Am.*, *76*, 1447–1460.

Ben-Zion, Y., and A. A. Allam (2013), Seasonal thermoelastic strain and postseismic effects in Parkfield borehole dilatometers, *Earth Planet. Sci. Lett.*, *379*, 120–126, doi:10.1016/j.epsl.2013.08.024.

Bertiger, W., S. D. Desai, B. Haines, N. Harvey, A. W. Moore, S. Owen, and J. P. Weiss (2010), Single receiver phase ambiguity resolution with GPS data, *J. Geodesy*, *84*(5), 327–337, doi:10.1007/s00190-010-0371-9.

Bettadpur, S. (2012), *Gravity Recovery and Climate Experiment UTCSR Level-2 Processing Standards Document for Level-2 Product Release 0005*, Center for Space Research, Univ. of Tex., Austin.

Blewitt, G., C. Kreemer, W. C. Hammond, and J. M. Goldfarb (2013), Terrestrial reference frame NA12 for crustal deformation studies in North America, *J. Geodyn.*, *72*, 11–24, doi:10.1016/j.jog.2013.08.004.

Borsa, A. A., D. C. Agnew, and D. R. Cayan (2014), Ongoing drought-induced uplift in the western United States, *Science*, *345*(6204), 1587–1590, doi:10.1126/science.1260279.

Boy, J. P., and F. Lyard (2008), High-frequency non-tidal ocean loading effects on surface gravity measurements, *Geophys. J. Int.*, *175*, 35–45, doi:10.1111/j.1365-246X.2008.03895.x.

Calcaterra, D., D. Ducci, and A. Santo (1994), Aspetti geomeccanici ed idrogeologici nel settore sud-orientale del monte Terminio (Appennino meridionale), *Geol. Romana*, *30*, 53–66.

Celico, P., and M. Civita (1976), Sulla tettonica del massiccio del Cervialto (Campania) e le implicazioni idrogeologiche ad essa connesse [On the tectonics of the Cervialto Massif (Campania) and related hydrogeological issues], *Boll. Soc. Natur. Naples*, *85*, 555–580.

Celico, P., L. Pelella, D. Stanzione, and S. Aquino (1994), Sull'idrogeologia e l'idrogeochimica dei Monti Alburni (SA), *Geol. Romana*, *30*, 687–698.

Celico, F., E. Petrella, and P. Celico (2006), Hydrogeological behaviour of some fault zones in a carbonate aquifer of southern Italy: An experimentally based model, *Terra Nova*, *18*, 308–313, doi:10.1111/j.1365-3121.2006.00694.x.

Chanard, K., J. P. Avouac, G. Ramillien, and J. Genrich (2014), Modeling deformation induced by seasonal variations of continental water in the Himalaya region: Sensitivity to Earth elastic structure, *J. Geophys. Res. Solid Earth*, *119*, 5097–5113, doi:10.1002/2013JB010451.

D'Agostino, N., J. A. Jackson, F. Dramis, and R. Funiciello (2001), Interactions between mantle upwelling, drainage evolution and active normal faulting: An example from the central Apennines (Italy), *Geophys. J. Int.*, *147*(2), 475–497, doi:10.1046/j.1365-246X.2001.00539.x.

D'Agostino, N. (2014), Complete seismic release of tectonic strain and earthquake recurrence in the Apennines (Italy), *Geophys. Res. Lett.*, *41*(4), 1155–1162, doi:10.1002/2014GL059230.

Dahle, C., F. Flechtner, C. Gruber, D. König, R. König, G. Michalak, and K. H. Neumayer (2012), GFZ GRACE Level-2 Processing Standards Document for Level-2 Product Release 0005, Scientific Tech. Rep. STR12/02 Data, 20 p., Potsdam: Deutsches GeoForschungsZentrum GFZ.

Del Prete, S., M. Manco, and F. Maurano (2007), *Aspetti speleogenetici della Grotta della Prufunnata (Monti Picentini, Campania)*, Atti I Convegno Regionale di Speleologia "Campania Speleologica", Oliveto Citra (SA).

De Vita, P., V. Allocca, F. Manna, and S. Fabbrocino (2012), Coupled decadal variability of the North Atlantic Oscillation, regional rainfall and karst spring discharges in the Campania region (southern Italy), *Hydrol. Earth Syst. Sci.*, *16*, 1389–1399, doi:10.5194/hess-16-1389-2012.

Devoti, R., D. Zuliani, C. Braitenberg, P. Fabris, and B. Grillo (2015), Hydrologically induced slope deformations detected by GPS and clinometric surveys in the Cansiglio Plateau, Southern Alps, *Earth Planet. Sci. Lett.*, *419*, 134–142, doi:10.1016/j.epsl.2015.03.023.

Dong, D., P. Fang, Y. Bock, M. K. Cheng, and S. Miyazaki (2002), Anatomy of apparent seasonal variations from GPS-derived site position time series, *J. Geophys. Res.*, *107*, 2075, doi:10.1029/2001JB000573.

Dziewonski, A., and D. L. Anderson (1981), Preliminary reference Earth model, *Phys. Earth Planet. Inter.*, *25*, 297–356, doi:10.1016/0031-9201(81)90046-7.

Edge, R. J., T. F. Baker, and G. Jeffries (1981), Borehole tilt measurements: Aperiodic crustal tilt in an aseismic area, *Tectonophys.*, *71*, 97–109, doi:10.1016/0040-1951(81)90052-4.

Evans, K., and F. Wyatt (1984), Water table effects on the measurement of Earth strain, *Tectonophysics*, *108*, 323–337, doi:10.1016/0040-1951(84)90242-7.
Farrell, W. E. (1972), Deformation of the Earth by surface loads, *Rev. Geophys.*, *10*(3), 761–797, doi:10.1029/RG010i003p00761.
Fiorillo, F. (2009), Spring hydrographs as indicators of droughts in a karst environment, *J. Hydrol.*, *373*(3–4), 290–301, doi:10.1016/j.jhydrol.2009.04.034.
Fiorillo, F. (2011), Tank-reservoir drainage as a simulation of the recession limb of karst spring hydrographs, *Hydrogeol. J.*, *19*, 1009–1019, doi:10.1007/s10040-011-0737-y.
Fiorillo, F. (2013), Spring hydrographs recession and analysis of the Caposele spring (southern Italy) during dry periods, *Ital. J. Eng. Geol. Environ.*, *1*, 51–64, doi:10.4408/IJEGE.2013-01.O-04.
Fiorillo, F., and A. Doglioni (2010), The relation between karst spring discharge and rainfall by cross-correlation analysis (Campania, Southern Italy), *Hydrogeol. J.*, *18*(8), 1881–1895.
Fiorillo, F., M. Pagnozzi, and G. Ventafridda (2015a), A model to simulate recharge processes of Karst Massifs, *Hydrol. Process.*, *29*, 2301–2314, doi:10.1002/hyp.10353.
Fiorillo, F., M. Petitta, E. Preziosi, S. Rusi, S. Esposito, and M. Tallini (2015b), Long term trend and fluctuations of karst spring discharge in a Mediterranean area (central-southern Italy), *Environ. Earth Sci.*, *74*, 153–172, doi:10.1007/s12665-014-3946-6.
Ford, D., and P. Williams (2007), *Karst Hydrogeology and Geomorphology*, Wiley, England.
Fu, Y., D. F. Argus, and F. W. Landerer (2015), GPS as an independent measurement to estimate terrestrial water storage variations in Washington and Oregon, *J. Geophys. Res. Solid Earth*, *120*, 552–566, doi:10.1002/2014JB011415.
Galloway, D. L., and T. J. Burbey (2011), Review: Regional land subsidence accompanying groundwater extraction, *Hydrogeol. J.*, *19*, 1459, doi:10.1007/s10040-011-0775-5.
Guglielmi, Y., F. Cappa, J. Rutqvist, C. F. Tsang, and A. Thoraval (2008), Mesoscale characterization of coupled hydromechanical behavior of a fractured-porous slope in response to free water-surface movement, *Int. J. Rock Mech. Min.*, *45*(6), 862–878, doi:10.1016/j.ijrmms.2007.09.010.
Hartmann, A., N. Goldscheider, T. Wagener, J. Lange, and M. Weiler (2014), Karst water resources in a changing world: Review of hydrological modeling approaches, *Rev. Geophys.*, *52*, 218–242, doi:10.1002/2013RG000443.
Hoffmann, J., D. L. Galloway, H. A. Zebker, and F. Amelung (2001), Seasonal subsidence and rebound in Las Vegas Valley, Nevada, observed by synthetic aperture radar interferometry, *Water Resour. Res.*, *37*(6), 1551–1566, doi:10.1029/2000WR900404.
Hurrell, J. W. (1995), Decadal trends in the North-Atlantic oscillation: Regional temperatures and precipitation, *Science*, *269*(5224), 676–679, doi:10.1126/science.269.5224.676.
Hurrell, J. W., and H. van Loon (1997), Decadal variations in climate associated with the North Atlantic Oscillation, *Clim. Change*, *36*, 301–336, doi:10.1007/978-94-015-8905-5-4.
Hurrell, J. W., Y. Kushnir, and M. Visbeck (2001), The North Atlantic Oscillation, *Science*, *291*(5504), 603–605, doi:10.1126/science.1058761.
Ingebritsen, S. E., and T. Gleeson (2015), Crustal permeability: Introduction to the special issue, *Geofluids*, *15*, 1–10, doi:10.1111/gfl.12118.
Jacob, T., J. Chéry, F. Boudin, and R. Bayer (2010), Monitoring deformation from hydrologic processes in a karst aquifer using long-baseline tiltmeters, *Water Resour. Res.*, *46*, W09542, doi:10.1029/2009WR008082.
Jean, J., U. Meyer, and A. Jäggi (2015), Combination of monthly gravity field solutions from different processing centers, in *EGU General Assembly 2015*, vol. 17, pp. 5879, Geophysics Research Abstract, Vienna, Austria.
King, N. E., et al. (2007), Space geodetic observation of expansion of the San Gabriel Valley, California, aquifer system, during heavy rainfall in winter 2004–2005, *J. Geophys. Res.*, *112*, B03409, doi:10.1029/2006JB004448.
Kustowski, B., A. M. Dziewoński, and G. Ekström (2007), Nonlinear crustal corrections for normal-mode seismograms, *Bull. Seismol. Soc. Am.*, *97*(5), 1756–1762, doi:10.1785/0120070041.
Lagler, K., M. Schindelegger, J. Böhm, H. Krásná, and T. Nilsson (2013), GPT2: Empirical slant delay model for radio space geodetic techniques, *Geophys. Res. Lett.*, *40*, 1069–1073, doi:10.1002/grl.50288.
Landerer, F. W., and S. C. Swenson (2012), Accuracy of scaled GRACE terrestrial water storage estimates, *Water Resour. Res.*, *48*, W04531, doi:10.1029/2011WR011453.
LeGrand, H. E., and V. T. Stringfield (1971), Water levels in carbonate rock terranes, *Ground Water*, *9*, 4–10, doi:10.1111/j.1745-6584.1971.tb03544.x.
Lisowski, M. (2007), Analytical volcano deformation source models, in *Volcano Deformation: Geodetic Monitoring Techniques*, edited by D. P. Bondel, pp. 279–304, Praxis, Chichester, U. K.
Longuevergne, L., N. Florsch, F. Boudin, L. Oudin, and C. Camerlynck (2009), Tilt and strain deformation induced by hydrologically active natural fractures: Application to the tiltmeters installed in Sainte-Croix-aux-Mines observatory (France), *Geophys. J. Int.*, *178*, 667–677, doi:10.1111/j.1365-246X.2009.04197.x.
López-Moreno, J. I., S. M. Vicente-Serrano, E. Morán-Tejeda, J. Lorenzo-Lacruz, A. Kenawy, and M. Beniston (2011), Effects of the North Atlantic Oscillation (NAO) on combined temperature and precipitation winter modes in the Mediterranean mountains: Observed relationships and projections for the 21st century, *Global Planet. Change*, *77*(1–2), 62–76, doi:10.1016/j.gloplacha.2011.03.003.
Maccaferri, F. (2010), Numericals and analogue models of fluid-filled fractures propagation in layered media: Application to dikes and hydrofractures, Dissertation thesis, Alma Mater Studiorum Univ. di Bologna, Dottorato di ricerca in Geofisica, 22 Ciclo.
Manga, M. (1999), On the timescales characterizing groundwater discharge at springs, *J. Hydrol.*, *219*, 56–69, doi:10.1016/S0022-1694(99)00044-X.
Melini D., P. Gegout, G. Spada, and M. King (2014), REAR—A Regional ElAstic Rebound calculator, User manual for version 1.0. [Available at: http://hpc.rm.ingv.it/rear.]
Menzies, C. D., D. A. H. Teagle, D. Craw, S. C. Cox, A. J. Boyce, C. D. Barrie, and S. Roberts (2014), Incursion of meteoric waters into the ductile regime in an active orogen, *Earth Planet. Sci. Lett.*, *399*, 1–13, doi:10.1016/j.epsl.2014.04.046.
Métois, M., N. D'Agostino, A. Avallone, N. Chamot-Rooke, A. Rabaute, L. Duni, N. Kuka, R. Koci, and I. Georgiev (2015), Insights on continental collisional processes from GPS data: Dynamics of the peri-Adriatic belts, *J. Geophys. Res. Solid Earth*, *120*, 8701–8719, doi:10.1002/2015JB012023.
Miller, S. A. (2008), Note on rain-triggered earthquakes and their dependence on karst geology, *Geophys. J. Int.*, *173*, 334–338, doi:10.1111/j.1365-246X.2008.03735.x.
Moore, D. S., G. P. McCabe, W. M. Duckworth, and S. L. Sclove (2003), The Practice of Business Statistics: Using Data for Decisions.
Okada, Y. (1985), Surface deformation due to shear and tensile faults in a half-space, *Bull. Seism. Soc. Am.*, *75*(4), 1135–1154.
Ouellette, K. J., C. de Linage, and J. S. Famiglietti (2013), Estimating snow water equivalent from GPS vertical site-position observations in the western United States, *Water Resour. Res.*, *49*, 2508–2518, doi:10.1002/wrcr.20173.

Pastori, M., D. Piccinini, L. Margheriti, L. Improta, L. Valoroso, L. Chiaraluce, and C. Chiarabba (2009), Stress aligned cracks in the upper crust of the Val dåĂŹAgri region as revealed by shear wave splitting, *Geophis. J. Int.*, *179*(1), 601–614, doi:10.1111/j.1365-246X.2009.04302.x.

Prawirodirdjo, L., Y. Ben-Zion, and Y. Bock (2006), Observation and modeling of thermoelastic strain in Southern California Integrated GPS Network daily position time series, *J. Geophys. Res.*, *111*, B02408, doi:10.1029/2005JB003716.

Preisig, G., F. J. Cornaton, and P. Perrochet (2014), Regional flow and deformation analysis of basin-fill aquifer systems using stress-dependent parameters, *Ground Water*, *52*, 125–135, doi:10.1111/gwat.12034.

Rebischung, P., J. Griffiths, J. Ray, R. Schmid, X. Collilieux, and B. Garayt (2012), IGS08: The IGS realization of ITRF 2008, *GPS Solut.*, *16*(4), 483–494, doi:10.1007/s10291-011-0248-2.

Roeloffs, E. A. (2001), Creep rate changes at Parkfield, California 1966–1999: Seasonal, precipitation induced, and tectonic, *J. Geophys. Res.*, *106*(B8), 16,525–16,547, doi:10.1029/2001JB000352.

Scherneck, H. (1991), A parametrized solid earth tide model and ocean tide loading effects for global geodetic baseline measurements, *Geophys. J. Int.*, *106*(3), 677–694, doi:10.1111/j.1365-246X.1991.tb06339.x.

Sakumura, C., S. Bettadpur, and S. Bruinsma (2014), Ensemble prediction and intercomparison analysis of GRACE time-variable gravity field models, *Geophys. Res. Lett.*, *41*, 1389–1397, doi:10.1002/2013GL058632.

Swenson, S. C. (2012), Grace Monthly Land Water Mass Grids NETCDF Release 5.0.: Ver. 5.0. PO.DAAC, CA, USA, doi:10.5067/TELND-NC005.

Swenson, S. C., and J. Wahr (2006), Post-processing removal of correlated errors in GRACE data, *Geophys. Res. Lett.*, *33*, L08402, doi:10.1029/2005GL025285.

Tapley, B. D., S. Bettadpur, J. C. Ries, P. F. Thompson, and M. Watkins (2004), GRACE measurements of mass variability in the Earth system, *Science*, *53*(5683), 503–505, doi:10.1126/science.1099192.

Tenze, D., C. Braitenberg, and I. Nagy (2012), Karst deformations due to environmental factors: Evidences from the horizontal pendulums of Grotta Gigante, Italy, *Boll. Geofis. Teor. Appl.*, *53*, 331–345, doi:10.4430/bgta0049.

Thornthwaite, C. W. (1948), An approach towards a rational classification of climate, *Geograph. Rev.*, *38*, 55–94.

Tregoning, P., and T. van Dam (2005), Atmospheric pressure loading corrections applied to GPS data at the observation level, *Geophys. Res. Lett.*, *32*, L22310, doi:10.1029/2005GL024104.

Tsai, V. C. (2011), A model for seasonal changes in GPS positions and seismic wave speeds due to thermoelastic and hydrologic variations, *J. Geophys. Res.*, *116*, B04404, doi:10.1029/2010JB008156.

Valty, P., O. de Viron, I. Panet, and X. Collilieux (2015), Impact of the North Atlantic Oscillation on Southern Europe water distribution: Insights from geodetic data, *Earth Interact.*, *19*(10), 1–16, doi:10.1175/EI-D-14-0028.1.

van Dam, T. (2010), NCEP derived 6-hourly, global surface displacements at 2.5 × 2.5 degree spacing, [Available at http://geophy.uni.lu/ncep-loading.html.]

Wahr, J., M. Molenaar, and F. Bryan (1998), Time variability of the Earth's gravity field: Hydrological and oceanic effects and their possible detection using GRACE, *J. Geophys. Res.*, *103*(B12), 30,205–30,229, doi:10.1029/98JB02844.

Wahr, J., S. A. Khan, T. van Dam, L. Liu, J. H. van Angelen, M. R. van den Broeke, and C. M. Meertens (2013), The use of GPS horizontals for loading studies, with applications to Northern California and southeast Greenland, *J. Geophys. Res. Solid Earth*, *118*, 1795–1806, doi:10.1002/jgrb.50104.

Wang, H. (2000), *Theory of Linear Poroelasticity With Applications to Geomechanics and Hydrogeology*, Princeton Univ. Press, Princeton, N. J.

Wanner, H., S. Brönnimann, C. Casty, D. Gyalistras, J. Luterbacher, c. Schmutz, D. B. Stephenson, and E. Xoplaki (2001), North Atlantic Oscillation—Concepts and studies, *Surv. Geophys.*, *22*, 321–381, doi:10.1023/A:1014217317898.

Watkins, M. M., and D. N. Yuan (2012), *GRACE JPL Level-2 Processing Standards Document for Level-2 Product Release 05*, GRACE 327–744, version 5.0, Jet Propul. Lab., Pasadena, Calif.

Wessel, P., and W. H. F. Smith (1998), New, improved version of Generic Mapping Tools released, *Eos Trans. AGU*, *79*(47), 579–579, doi:10.1029/98EO00426.

Williams, S. D. P. (2008), CATS: GPS coordinate time series analysis software, *GPS Solut.*, *12*(2), 147–153, doi:10.1007/s10291-007-0086-4.

Wolfe, J., E. Berg, and G. Sutton (1981), The change in strain comes mainly from the rain: Kipapa, Oahu, *Bull. Seism. Soc. Am.*, *71*(5), 1625–1635.

Zhang, L., Z. Lu, X. L. Ding, H. S. Jung, G. C. Feng, and C. W. Lee (2012), Mapping ground surface deformation using temporarily coherent point SAR interferometry: Application to Los Angeles Basin, *Remote Sens. Environ.*, *117*, 429–439, doi:10.1016/j.rse.2011.10.020.

Zumberge, J., M. Heflin, D. Jefferson, M. Watkins, and F. Webb (1997), Precise point positioning for the efficient and robust analysis of GPS data from large networks, *J. Geophys. Res.*, *102*(B3), 5005–5017, doi:10.1029/96JB03860.